Wearable sweat sensors flexible PCB circuit design

by

Ying Song

Instructor:	Dr.Alina Rwei, Dr.Dante Malatore
Thesis committee:	Dr.Filipe Arroyo Cardoso
Daily supervisor:	Lena Fasching
Project Duration:	11, 2024 - 10, 2025
Faculty:	Faculty of Electrical Engineering, Mathematics and Computer Science (EEMCS), in collaboration with Faculty of Applied Sciences, Department of Chemical Engineering

TU Delft

Preface and Acknowledgements

This Master's thesis has been, for me, above all a journey toward a more complete understanding of circuit and PCB design. My very first encounter with microcontrollers and PCB dates back to my undergraduate studies, when I joined a robot-car competition. Together with my teammates, we had to build our knowledge base from scratch. This hands-on experience felt very different from theoretical analysis: holding real circuit boards in my hands, seeing the robot car move — and fail repeatedly — gave me a strong drive to improve and succeed. As a result, I chose to design PCB and coding for my undergraduate thesis. That project allowed me to revisit embedded systems principles. However, my focus remained mostly on programming and completing the PCB workflow, rather than on independently designing the circuits themselves.

At TU Delft, I shifted perspectives and learned analog circuit design from a microelectronics point of view. When it came time chose chip design. At first, I felt uncertain. Then I discovered this sweat-sensor PCB project. I realized that I still wanted to return to PCB design — I was not ready to leave behind that part of my undergraduate journey. I wanted to continue the path I had started, to master the skills I had not yet fully learned, and to turn my earlier attempts into competence.

Over the past year, this project has allowed me to do exactly that. From conducting the literature review, designing and modifying the circuits, designing the PCB layouts, coordinating fabrication details, programming the firmware, to testing the system and working with flexible substrates — I have gained a much deeper understanding of the entire process. For me, this thesis represents both a beautiful ending and a new beginning in my hardware design journey. In the future, I hope to continue working as a hardware engineer, building on this experience to further refine my circuit-design skills and grow as a professional.

Regarding my graduation project, I would like to express my heartfelt thanks to Lena for her kind encouragement throughout this journey. I am deeply grateful to Dr. Alina Rwei and Dr. Dante Muratore for their guidance and support. I also want to thank Ronald and Brian for their kind help when I faced issues with my circuit board — this project would not have been possible without all your support.

Looking back on my entire master's journey, I am endlessly thankful to my parents. When I was overwhelmed by financial pressure and questioned whether this degree was worth for many many time, they comforted me with warmth: telling me not to worry about money, not to push myself too hard, and that it was enough to simply eat well, rest well, and take care of my health. They never placed pressure on me — only unconditional support.

I also feel especially thankful for several dear friends. They listened to my self-doubt, shared the pressure with me, and walked alongside me during tough times. Chali always appeared just when I needed someone to talk to, bringing calm and laughter back to my heart. Yao Yuan and Li Jiayue have been with me through most of this master's degree — we have always been on the same wavelength, sharing academic stress and complaining about the environment together. This sense of companionship gave me a strong feeling of belonging.

Zhang Dingyue was my closest companion during Q1. After arriving alone in the Netherlands, she was my very first friend. We visited each other's rooms and spent Christmas together. That half year was filled with joy. Even after she returned to China, we continued to talk for a long time.And to everyone else who showed up in my life, I also want to say thank you — for your presence and conversations: Linlin, Fengfeng, Awu, Box, Lucas, Momin, Panpan, and Daijun.

Ying Song
Delft, October 2025

Summary

Flexible wearable sweat sensors can monitor sweat continuously and non-invasively in real time. They give useful information about the human body at the molecular level. Because of their high performance, low cost, and small size, electrochemical sensors have received much attention for use in personal health monitoring.

In this thesis, a back-end electronic system for a flexible electrochemical sweat sensor is developed with several key modules for stable and accurate monitoring. The work begins with a review of recent studies on wearable sweat sensing, focusing on ion-selective electrodes, iontophoresis, impedance measurement, and system integration methods. Then, the overall system design is introduced, including schematic and layout planning, and main circuit blocks such as power management, iontophoresis for sweat induction, and impedance measurement using the AD5933 chip. Firmware and data collection with an STM32 microcontroller are also described, covering signal sampling, impedance readout, and Bluetooth communication.

The experimental part presents the validation of the first prototype, showing the main functional tests, the problems found, and their solutions in the second-version PCB. The MCU, power management, Bluetooth communication, and iontophoresis modules operated reliably, while the ISE readout and impedance measurement using the AD5933 were only partially successful. The second-version PCB is built on a flexible polyimide substrate with local stiffeners, forming a ridge-flex bridge structure. This design improves both mechanical strength and flexibility for wearable use.

Contents

Preface i

Summary ii

Nomenclature v

1 Introduction 1

2 Theoretical backgound 3
- 2.1 Sweat Induction Methods 3
  - 2.1.1 Passive and Active Methods 3
  - 2.1.2 Iontophoresis 3
  - 2.1.3 Circuit Design for Iontophoresis 4
- 2.2 Ion-Selective Electrodes 5
  - 2.2.1 Introduction to Ion Selective Electrodes (ISE) 5
  - 2.2.2 Circuit Implementation for ISE 6
- 2.3 Sweat flow rate sensor 6
- 2.4 Flexible Substrates for Wearable PCB 7
  - 2.4.1 Material Options for Wearable PCBs 7
- 2.5 Power Supply 8

3 System Architecture and Circuit Design 9
- 3.1 Overall System Architecture 9
- 3.2 ISE Potenial Signal Acquisition and Amplification Circuit 9
  - 3.2.1 Architecture choice 9
  - 3.2.2 Gain design ADC Matching 11
  - 3.2.3 Filtering Noise Analysis 11
  - 3.2.4 Power management for AD8237 13
- 3.3 Iontophoresis Voltage-Controlled Current Source Design 14
  - 3.3.1 Design Principle 14
  - 3.3.2 Simulation Verification 15
- 3.4 Impedance Measurement Circuit 16
  - 3.4.1 AD5933 Functional Diagram Overview 16
  - 3.4.2 Measurement Circuit Design and Calibration 16
  - 3.4.3 Dual-Path Measurement Strategy 16
- 3.5 MCU Integration 17
- 3.6 Power management Circuit Design 17

4 PCB Layout Design and Firmware 19
- 4.1 PCB Layout Strategies 19
  - 4.1.1 PCB Layout Overview 19
  - 4.1.2 Grounding Strategy 19
  - 4.1.3 Signal Routing Principles 20
  - 4.1.4 Decoupling and Power Integrity 20
- 4.2 Firmware Architecture and working Principle 21
  - 4.2.1 Data Acquisition and Control 21
  - 4.2.2 Wireless communication and Data package 22

5 Results and Discussion 23
- 5.1 Functional verification of subsystems 23
  - 5.1.1 Validation of main control unit and Power management 23
  - 5.1.2 Iontophoresis circuit testing 24

5.2 Experimental challenges and limitations 25
5.2.1 Ion-selective electrode (ISE) module analysis 25
5.2.2 AD5933 sweat rate impedance measurement 26

6 Future Work and Conclusion **28**
6.1 Future Work 28
6.1.1 Design Principles for Rigid–Flex Wearable PCBs 28
6.1.2 Flexible PCB V2 Layout and Mechanical Design 28
6.2 Conclusion 30

References **31**

A Appendix **37**

Nomenclature

Abbreviations

Abbreviation	Definition
ADC	Analog-to-Digital Converter
BLE	Bluetooth Low Energy
CCR	Capture/Compare Register
DAC	Digital-to-Analog Converter
DC	Direct Current
DDS	Direct Digital Synthesis
DMA	Direct Memory Access
DFT	Discrete Fourier Transform
DUT	Device Under Test
EMI	Electromagnetic Interference
GPIO	General-Purpose Input/Output
I^2C	Inter-Integrated Circuit
ISE	Ion-Selective Electrode
LDO	Low Dropout Regulator
MCU	Microcontroller Unit
PCB	Printed Circuit Board
PWM	Pulse Width Modulation
UART	Universal Asynchronous Receiver–Transmitter
VOUT	Voltage Output

Symbols

Symbol	Definition	Unit
V	Voltage	[V]
I	Current	[A]
R	Resistance	[Ω]
Z	Impedance	[Ω]
G	Amplifier gain or AD5933 gain factor	[–]
D	PWM duty cycle	[%]
R_{FB}	Feedback resistor (AD5933)	[Ω]
R_{CAL}	Calibration resistor	[Ω]
R_{LIM}	Limiting resistor (current control)	[Ω]
f	Frequency	[Hz]
f_{start}	Start frequency (AD5933)	[Hz]
F_{system}	System clock frequency	[Hz]
N	Resolution bits (e.g. ADC)	[–]
V_{ref}	Reference voltage (ADC)	[V]
$V_{n,\mathrm{rms}}$	RMS voltage noise	[V]
BW	Bandwidth	[Hz]
SNR	Signal-to-noise ratio	[dB]

1

Introduction

Traditional health monitoring methods rely on invasive blood sampling and clinical tests. These procedures can cause discomfort and make continuous monitoring difficult.

Wearable sensors offer a non-invasive solution for real-time and continuous health monitoring during daily activities [1]. They have great potential for predictive analysis, personal health tracking, and early medical intervention. However, most current devices only record physical activity and vital signs, such as heart rate, and cannot show health information at the molecular level.

To obtain molecular-level data in a non-invasive way, sweat is an ideal biofluid because it contains many biomarkers that reflect body conditions, including electrolytes, metabolites, hormones, proteins, and peptides [2][3]. Heikenfeld et al. [4] and Moyer et al. [5] have shown that some analytes in blood are closely related to chemical levels in sweat, suggesting that sweat can serve as a useful and non-invasive alternative for personal health monitoring.

Sweat is produced by glands distributed across the body. It can be collected non-invasively from suitable skin areas, allowing fast detection before analytes start to degrade. Continuous sweat collection during daily activities can strongly support precision medicine by enabling long-term molecular monitoring. As an example, Figure 1.1 shows a fully integrated sweat sensor platform developed by Wei Gao et al., which demonstrates the potential for small size and good wearability.

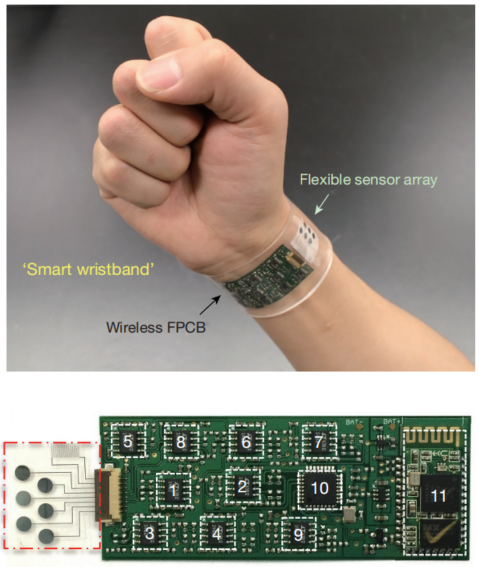

Figure 1.1: A fully integrated wearable sensing platform using PET as the substrate[6]

The integration of iontophoresis technology allows for the active induction of sweat in non-active scenarios, effectively aiding in the continuous monitoring of various health conditions. This is particularly important for patients who may not be able to engage in physical activity, such as the elderly, infants, or those who are ill [7]. Moreover, the adoption of microfluidic technology significantly boosts data integrity by allowing for continuous and quantitative analysis of freshly secreted sweat. This technology ensures that each sweat sample is new and not mixed with older secretions, eliminating delays and inaccuracies in sweat data.[8] Altogether, these technological advancements improve sweat collection and sample transport, greatly increasing both the temporal resolution and the precision of sweat analyte analysis in wearable devices.

In this thesis, a flexible electrochemical sweat sensor system is developed, focusing on the electronic circuit and PCB design. The aim of the research is to create a small, integrated, and wearable platform that can continuously and non-invasively monitor sweat analytes. The work concentrates on the electronic part of the system and explores how each sensing concept can be achieved through circuit implementation.

The designed PCB integrates five main modules: an ion-selective electrode (ISE) readout for electrolyte measurement, an iontophoresis circuit for active sweat induction, an impedance sensing module for sweat rate detection, power management, and a microcontroller unit for data processing and transmission. These circuits are built on a polyimide-based flexible PCB to ensure wearability and comfort. The system is compact and portable, integrating the MCU and bluetooth for wireless communication. The ISE readout detects small voltage differences with high accuracy and low noise, the iontophoresis module delivers a stable and controlled microcurrent, and the impedance sensing tracks changes in sweat flow rate for real-time monitoring.

2

Theoretical backgound

2.1. Sweat Induction Methods

2.1.1. Passive and Active Methods

There are two main methods for collecting sweat samples: passive methods and active methods. Passive methods involve inducing sweat secretion through vigorous physical activity such as running, cycling or other forms of exercise,as the Figure 2.1 or exposure to heat [9]. However, for sedentary people, it is not possible to directly obtain enough sweat for real-time analysis, which limits our ability to perform such non-invasive and real-time analysis of various biomarkers[10]. Therefore, an active method uses electrical stimulation, iontophoresis.

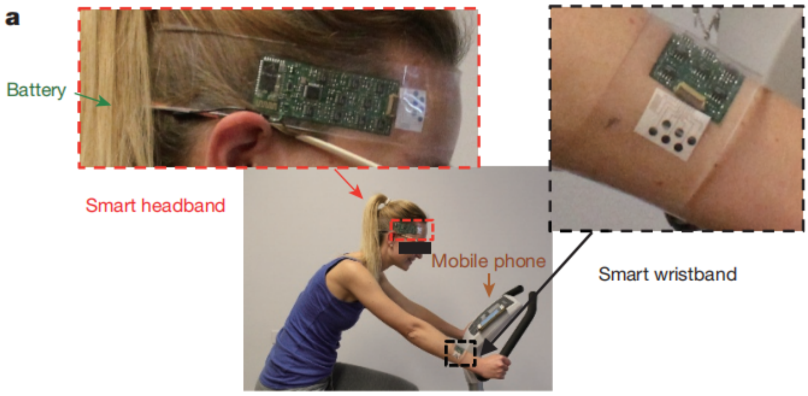

Figure 2.1: Passive Methods for induce sweat.[11]

2.1.2. Iontophoresis

Iontophoresis is a commonly used method to stimulate local sweat secretion in selected skin areas. However, the traditional iontophoresis procedure involves several steps, such as stimulation, off-skin collection, and laboratory analysis of sweat. These steps require manual handling and do not allow real-time monitoring of the secretion process.

As shown in Figure. 2.2, iontophoresis applies a small voltage to two electrodes placed on the skin surface: an anode and a cathode. The applied voltage generates an electric current beneath the skin, which drives sweat-inducing agents, such as pilocarpine, into the sweat glands near the anode and triggers sweat secretion.

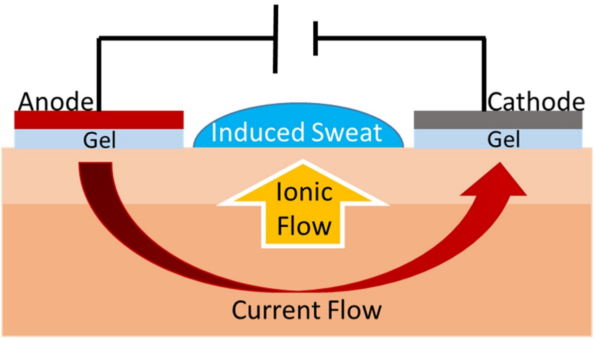

Figure 2.2: The basic principle of iontophoresis[12]

2.1.3. Circuit Design for Iontophoresis

The proper design of iontophoresis circuits is important for accurate control of how therapeutic agents are delivered through the skin. Iontophoresis depends on the circuit's ability to provide a constant and stable current that drives charged molecules across the skin barrier [13]. This section explains the main circuit parts, their roles, and the safety features needed to ensure both effective and safe operation. Topics range from power supplies that provide a steady current to feedback systems that monitor voltage in real time.

First, the power supply should provide a stable current, since the performance of iontophoresis depends on keeping the current at a fixed level. Typically, iontophoresis is performed with low current densities below $0.5\,\mathrm{mA/cm^2}$ to ensure safety and comfort [14]. The skin, as a biological interface, has an electrical impedance that is not only dynamically variable and inter-individually variable, typically ranging from 1 to $20\,\mathrm{k\Omega{\cdot}cm^2}$ under hydrated or gel-contact conditions, and can exceed $100\,\mathrm{k\Omega{\cdot}cm^2}$ for dry skin [15, 16]. This means that the skin's impedance to current may vary from person to person and from one person to another at different times.

The constant-current source must handle changes in skin impedance to avoid too much current, which can damage the skin, or too little current, which can reduce drug delivery. According to Ohm's law, to keep a steady current through the skin, the circuit needs to change the applied voltage when the skin resistance varies. When the resistance is high, a higher voltage is needed to keep the same current [17].

Compliance voltage is the maximum voltage that a power supply or current source can adapt itself to and deliver at a constant current output[18]. The main function of the compliance voltage is to ensure that the current source can maintain the set current constant when the load resistance changes. Since changes in resistance can affect current, the level of compliance voltage directly determines how much of a resistance range the current source can handle. In iontophoresis, such as the delivery of sweat-inducing drugs (e.g. carbachol) through the skin, the resistance of the skin is highly variable[19]. Initially, the resistance of the skin may be high, and as the treatment progresses, the resistance decreases due to increased skin permeability. If the compliance voltage is too low, it may not be able to overcome the high resistance, resulting in a drop in current, which may affect the effectiveness of the treatment[11].

While a high compliance voltage ensures constant current delivery, it also increases the risk that, if not properly controlled, excessive current could flow through the skin and cause tissue damage. Therefore, continuous current monitoring and feedback control are essential to maintain safe operation. Emaminejad et al. implemented a programmable current source to induce sweating periodically with integrated current monitoring and safety mechanisms[11].Their design (Fig.2.3) shows how programmable iontophoresis currents can be controlled while keeping the user safe with current limiting and fault isolation. In this project, the same concept is implemented on a flexible PCB, combining programmable iontophoresis and sensing modules with current monitoring for safety.

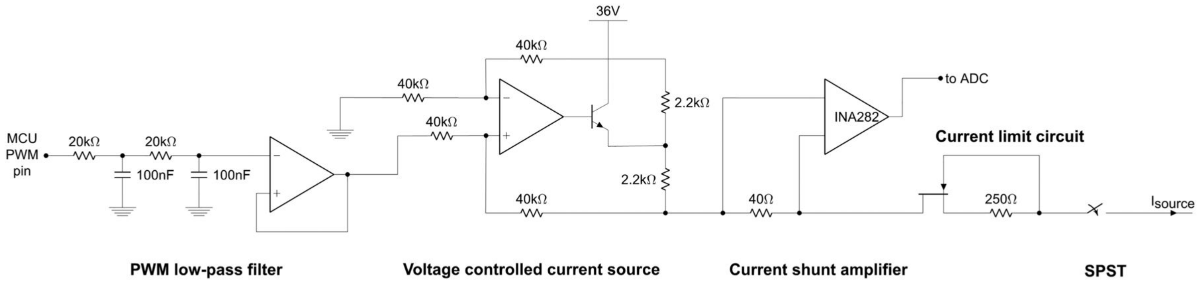

Figure 2.3: Current delivery circuit schematic diagram [11].

2.2. Ion-Selective Electrodes

2.2.1. Introduction to Ion Selective Electrodes (ISE)

Sweat sensors need to be selective to electrolytes because ion concentrations in sweat not only have direct physiological meaning but also affect the conductivity of sweat, which can influence the accuracy of electrochemical sensor readings. An ion-selective electrode (ISE) [20], also called a specific ion electrode (SIE), is a sensor that converts changes in the concentration of specific ions into an electrical potential, shown in the fig2.4.

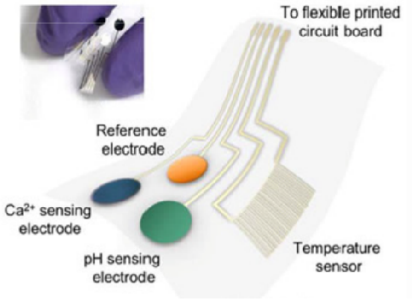

Figure 2.4: A fully integrated wearable wristband that could detect Ca2+ and pH at the same time.[21]

An ISE comprises two parts: a working electrode with a selective membrane that provides chemical selectivity for the target ion, and a reference electrode that supplies a stable reference potential. The selective membrane can be implemented as glass, solid-state, liquid-membrane, or composite designs[22]. The reference electrode is commonly Ag/AgCl embedded in a chloride-saturated polymer matrix, ensuring a stable potential for differential measurement[23].

When the target ion interacts with or passes the selective membrane, a potential develops across the membrane due to differences in ionic activity on the two sides. The working electrode measures this potential relative to the reference electrode, and the measured potential varies logarithmically with the ion's activity according to the Nernst equation[24]:

$$E = E_0 + \frac{RT}{zF} \ln([\text{Ion}]) \tag{2.1}$$

where E is the cell potential, E 0 is the standard potential, R is the universal gas constant, T is the absolute temperature, z is the charge of the ion, F is the Faraday constant, and [Ion] is the activity of the ion. Based on the Nernst equation, the theoretical potential response limit of the ISE is approximately 59.2 mV per tenfold change in target analyte concentration at 25 °C[25]. The overall cell potential of an ISE system can be described as:

$$E = E_M + E_{\text{ref}} + E_{\text{const}} \tag{2.2}$$

where E_M is the membrane potential arising from the ion-selective membrane, E_{ref} is the junction potential of the reference electrode, and E_{const} represents all other constant contributions. By combining the ion-selective membrane with a stable reference electrode, the open-circuit potential of the ISE can be measured.

2.2.2. Circuit Implementation for ISE

Open Circuit Potential Technique (OCPT) has become one of the most commonly used electrochemical technologies in wearable sweat sensors due to its simplicity and low power consumption[26]. OCPT is typically employed for the selective detection of sweat electrolytes, requiring a high-impedance voltmeter to measure the potential between the reference electrode and the working electrode. Due to the potentially high source impedance of the potential sensors, they must be connected to a high input impedance voltage buffer to minimize the current flowing through the electrodes[27]. The reference electrode provides a stable potential, which is preserved by a high-input-impedance buffer to avoid loading effects[28]. This potential is captured by an ADC, allowing one to determine the ion concentration in sweat based on the Nernst equation. For the measurement of sweat electrolytes, the sensor response is usually stable. Therefore, a low-bandwidth signal path (for example, with a -3 dB cut-off frequency of 1 Hz [6]) and standard ADC sampling intervals are sufficient to satisfy the requirements for continuous monitoring. This design approach enables instruments that are low in power consumption and compact in size.

2.3. Sweat flow rate sensor

Sweat flow rate is the amount of sweat produced in a given time. It is important for evaluating body hydration and for correctly understanding sweat biomarker data[29]. The composition of sweat changes with the sweat rate: when the rate is high, electrolytes such as sodium and chloride increase; when the rate is low, metabolites like lactate and urea become more concentrated[30]. However, sweat is produced only in small amounts, so wearable sensors need to collect and guide it efficiently. Modern devices use microfluidic collectors that move sweat through small channels without extra power[31]. This method allows continuous collection of fresh sweat and helps prevent evaporation and contamination[32]. In the past, sweat rate was measured by large systems such as body weight tracking, absorbent pads, or humidity sensors, which could only be used in the lab[33]. In contrast, on-skin microfluidic sensors make it possible to monitor sweat rate continuously and in real time. One useful method for measuring sweat flow is to place capacitive or impedance sensors inside the microchannels[21]. When sweat moves forward, it changes the dielectric property of the channel and forms a conductive path between the electrodes. This leads to changes in impedance or capacitance. By matching these signal changes with sweat volume or flow distance, the device can measure sweat rate in real time. For instance, Nyein et al.[21] designed a wearable patch with a spiral microchannel placed over interdigitated electrodes to monitor sweat flow, as shown in Figure 2.5.

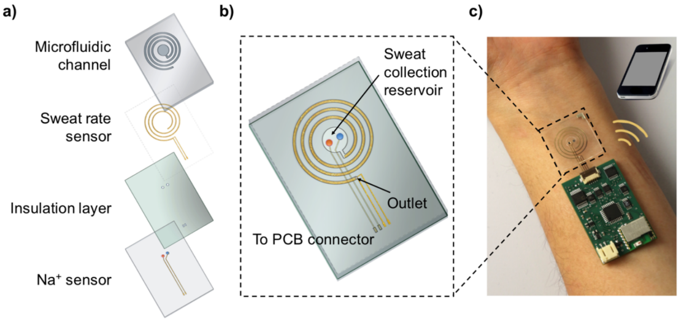

Figure 2.5: Schematics of a wearable sweat sensing patch integrating a spiral microfluidic channel with interdigitated Au electrodes.[21]

Sweat flow can be measured by tracking how moving sweat changes the dielectric environment and creates a conductive path between electrodes. The increase in admittance or capacitance can be calibrated to estimate flow rate in real time. This concept has been demonstrated in several on-skin devices. Nyein et al.[21] developed a spiral microchannel with interdigitated electrodes, where advancing sweat caused admittance to rise and matched syringe-pump flow references. Choi et al.[34] presented a simple parallel-plate capacitive sensor with a linear response to channel filling, consistent with the Macroduct collector. More recently, Moonen et al.[35] introduced a droplet-based method in which nanoliter droplets generate clear capacitance steps, allowing very low sweat rates to be detected. A typical impedimetric layout is illustrated in Figure 2.6, showing a spiral microchannel with interdigitated electrodes where the advancing sweat front changes the measured impedance or admittance. Despite these advances, several practical challenges remain. First, microchannels have limited capacity; once they are filled, new sweat cannot be measured until the liquid is removed or absorbed[21]. Second, changes in sweat ion concentration affect conductivity and can cause signal drift that is not related to volume. To correct this, calibration or simultaneous ion measurement may be needed[11]. In this work, the system combines sweat rate sensing with ion concentration measurement to address this issue.

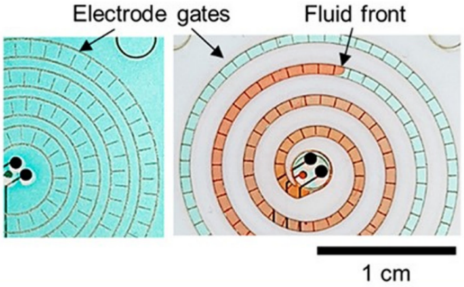

Figure 2.6: Spiral microchannel with interdigitated electrodes (IDEs) for impedimetric sweat-flow sensing.[36]

2.4. Flexible Substrates for Wearable PCB

Wearable electronic devices require flexible PCB substrates to remain comfortable and conform to the body. Traditional rigid FR4 cannot bend over curved surfaces and may cause discomfort or mechanical stress during use[37]. In contrast, thin flexible films such as polyimide (PI) can move with the skin and maintain stable contact, making the device light and patch-like for daily wear[38]. PI is also biocompatible, allowing safe and long-term contact with skin. For example, Petrelli et al.[39] demonstrated a PI-based circuit with CNT sensors (Figure 2.7) for sweat ammonium detection, which maintained stable performance under bending. Flexible PCBs are not only more comfortable but also more reliable during motion. A rigid board may crack or detach, whereas a flexible circuit can bend repeatedly without damage[40]. This ability to follow body contours is an essential feature for modern wearable systems.

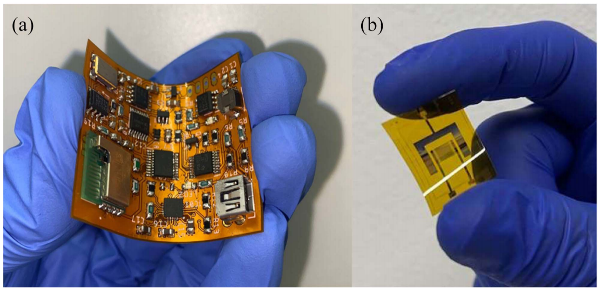

Figure 2.7: Examples of flexible PCB substrates used in wearable biosensing applications. (a) Flexible readout circuit with surface-mounted ICs. (b) Thin-film polyimide-based sensing substrate. Adapted from [39].

2.4.1. Material Options for Wearable PCBs

Among flexible substrates, polyimide (PI) is widely used[41]. It has high thermal stability, chemical resistance, and mechanical strength, while being thin and flexible. Importantly, PI can survive soldering temperatures above 250 °C and is compatible with PCB processes[42]. These properties make PI the best choice for most wearable circuits, though it is more expensive than alternative polymers such as PET. Thin PI films (for example, 25 µm) allow very low device profiles and tight bending, enabling patch-like wearables. However, very thin layers can be fragile and may require reinforcement in specific areas. Other polymers have limits. PET is cheap and transparent, but softens at 120–150 °C, so it cannot handle standard soldering temperatures[43]. PEN performs slightly better but still shows lower thermal stability than PI. These are mainly used in simple, low-cost circuits. Elastomers such as polydimethylsiloxane (PDMS) or polyurethane are highly stretchable, but degrade at soldering temperatures and are hard to pattern with fine copper traces[44]. In summary, PI offers the best balance of flexibility, strength, and manufacturability and is the standard substrate for wearable PCB design. Other materials have been explored, but remain limited to niche or research uses.

2.5. Power Supply

In wearable devices, parts such as data processors and wireless modules need continuous and stable power. Therefore, the power supply is an important part of the whole system design.

Several energy options have been studied. Solar cells can turn sunlight into electricity, and triboelectric nanogenerators (TENGs) can collect mechanical energy from body motion[45, 46, 47]. Biofuel cells can also take energy directly from human sweat, showing high power density in body fluids and long operation during exercise[48]. These methods are promising for future wearable devices, but they still have limits in stability, efficiency, and system integration. For now, they are mainly used as supporting power sources rather than the main supply.

Different types of batteries have also been developed. Stretchable lithium-based batteries on flexible substrates aim to improve both safety and flexibility, while zinc–manganese batteries offer light weight and high capacity[49, 50]. However, these new designs are still in the early stage and are not yet widely used.

At present, lithium-ion batteries are the most practical option. They provide high energy density, long lifetime, and fast charging speed[51]. Although there are concerns about size and safety, small lithium-ion batteries remain reliable, low-cost, and easy to replace. Therefore, in this work, a single 3.7 V lithium-ion battery is used as the main power source.

3

System Architecture and Circuit Design

3.1. Overall System Architecture

To explain the design clearly, this section introduces the overall system before describing each circuit block in detail. The system is built in a modular way, so each sensing and control part can be developed and tested separately while still working well together on the PCB. Figure 3.1 shows the architecture of the wearable sweat sensing system. The device includes three main sensing modules and a central microcontroller unit (MCU):

- **Iontophoresis Module:** Generates a controlled 0–1.5 mA constant current for 5 min every 3 hour. It actively induce sweat secretion at the skin interface.
- **Ion-Selective Electrode (ISE) Module:** Acquires 80-300 mV signals from working and reference electrodes, with resolution 0.1 mV.
- **Sweat Rate (Impedance) Module:** Measures skin-electrode impedance in the 1 kΩ–100 kΩ range, enabling real-time estimation of sweat flow rate.
- **STM32 MCU:** Coordinates module operation via PWM, ADC, and I^2C interfaces. It processes the collected data and sends the results through UART to a BLE module for wireless transmission.
- **Power Management:** A 3.7,V Li-ion battery supplies a set of voltage regulators that generate 36,V, 5,V, and 3.3,V rails.

To match the signal level of ion-selective electrodes, we set the input voltage range of our circuit to 80–300mV. The typical value is around 200mV. This choice is supported by Gao et al.[6], who found open-circuit voltages between 0.1–0.3V in their wearable Na and K sensors. Yang et al.[52] also reported similar results, with printed ISEs showing base voltages close to 200mV.

For sweat stimulation, we used iontophoresis current between 0 and 1.5mA. This range follows medical practice. Gokdemir and Karadag [53] explained that 1.5mA is a safe current used in sweat tests. Reynaerts et al. [54] also showed that 1.5mA can effectively make sweat using a commercial device. These works support our settings for both voltage and current in the sweat sensor design.

3.2. ISE Potenial Signal Acquisition and Amplification Circuit

3.2.1. Architecture choice

The ion-selective electrode (ISE) produces an open-circuit potential typically in the range of 80–300 mV, depending on the ionic composition of sweat. This potential is directly related to the concentration of target ions and thus serves as the main sensing signal. However, a key challenge for ISE-based sensors is that the electrode interface has very high source impedance, often in the range of megaohms or more. If the measurement circuit does not have enough input impedance, even a small current drawn from

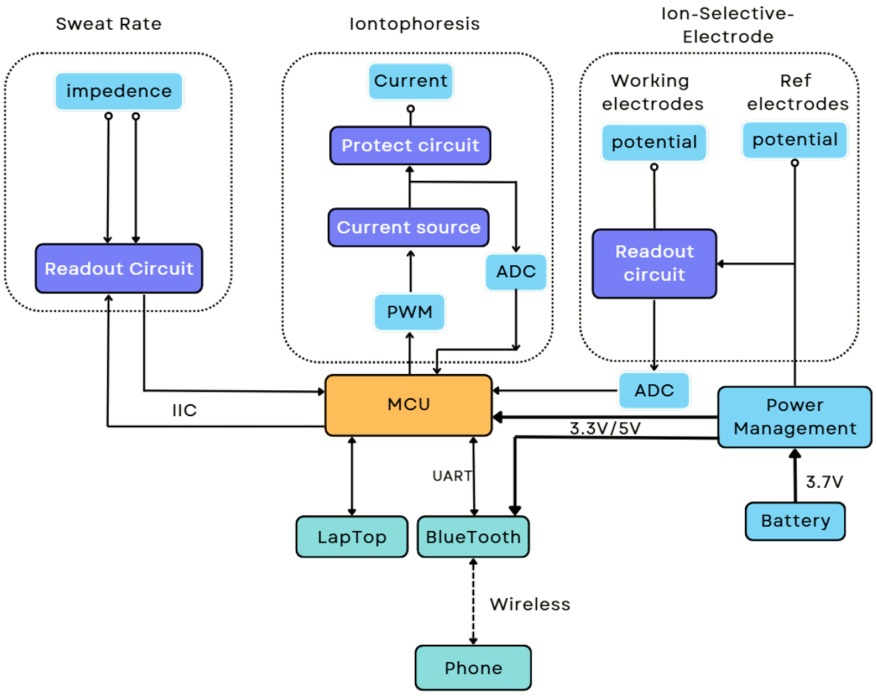

Figure 3.1: High-level block diagram of the integrated wearable sweat sensing system.

the electrode can disturb the electrochemical balance. This effect, known as electrode polarization, causes signal drift and reduces measurement stability[55]. To solve this problem, an open-circuit measurement method is used. The essential principle is to sense the electrode voltage without letting current flow through the interface. In practice, this needs a measurement front-end with very high input impedance, ideally in the gigaohm range. With almost zero current, the electrode potential can be measured accurately without polarization effects, ensuring signal accuracy and stability.

In previous work of Gao's group [6], the signal chain for sweat sensing was structured in three sequential stages:

- A **voltage buffer** with ultra-high input impedance, preventing loading of the ISE and enabling stable open-circuit potential measurement.
- A **differential amplifier**, which subtracts the reference electrode potential from the working electrode potential, thereby extracting the true sensing signal while rejecting common-mode interference.
- A **low-pass filter**, designed to attenuate high-frequency noise originating from motion or environmental fluctuations, so that the low-frequency ion signal remains intact.

This three-block architecture has been widely adopted in bioelectrochemical sensor systems, as it clearly addresses the main requirements of high input impedance, differential measurement, and noise suppression. However, using separate buffer and amplifier circuits adds more components, which can increase noise and make the circuit more complex. In this design, these functions are combined into a single instrumentation amplifier (IA). The IA includes two high-input-impedance buffer stages and one precision differential amplifier inside the same chip. This setup keeps the advantages of the original three-stage design while reducing the number of parts. As a result, the circuit becomes more compact and is designed to improve noise performance and common-mode rejection.

Following the IA stage, the conditioned signal passes through a fourth-order active low-pass filter to further reduce unwanted noise before being digitized by the microcontroller's ADC. An overview of this whole readout path is shown in Figure 3.2. This system ensures that the small signals from the sweat–electrode interface are measured accurately and processed reliably.

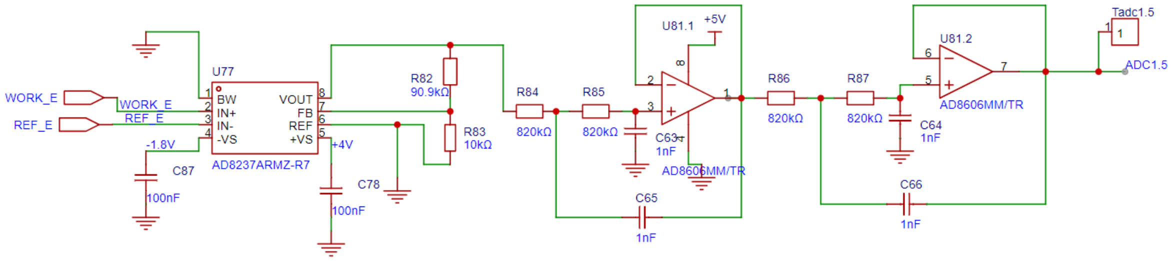

Figure 3.2: Schematic overview of the signal acquisition and amplification circuit.

3.2.2. Gain design ADC Matching

After the initial acquisition stage, the sweat signal usually appears as a weak electrochemical potential difference with an amplitude between 80 mV and 300 mV, typically around 200 mV. Feeding such a low-voltage signal directly into the microcontroller ADC would lead to poor quantization resolution, making it difficult to achieve high measurement precision. Therefore, the signal must be amplified to make full use of the ADC's input range.

Considering the needs for performance, precision, and low power, the AD8237 instrumentation amplifier was chosen as the main amplification stage. Compared with general-purpose operational amplifiers, an instrumentation amplifier includes high-input-impedance buffers and a precise differential amplifier. This design offers two main advantages: it prevents polarization effects caused by low input impedance at the sensor interface and reduces common-mode noise, improving signal quality and measurement stability.

According to the ADC specifications of the STM32F1 microcontroller, the built-in 12-bit ADC operates within an input range of 0–3.3 V. Therefore, the gain of the instrumentation amplifier was set to 10. With a maximum input signal of about 300 mV, the amplified output reaches around 3 V, which is close to the ADC reference voltage and makes full use of its quantization range. Using the full ADC range improves resolution and reduces relative quantization error.

For a 12-bit ADC, the number of quantization levels is:

$$2^{12} = 4096$$

Thus, the least significant bit (LSB) size is:

$$\text{LSB} = \frac{3.3\,\text{V}}{4096} = 0.0008057\,\text{V} = 805.7\,\mu\text{V}$$

Considering the signal has been amplified by 10, the equivalent input-referred resolution becomes:

$$\frac{805.7\,\mu\text{V}}{10} = 80.57\,\mu\text{V}$$

The input-referred resolution of about 0.08 mV exceeds the design target of 0.1 mV. Even when considering real-world effects such as component tolerance and noise, the system can still provide stable and accurate measurements with at least 0.1 mV precision. This resolution is sufficient to detect small changes in ion concentration in sweat and supports reliable monitoring of physiological parameters.

3.2.3. Filtering Noise Analysis

To achieve high-precision signal acquisition, the noise performance of the analog front end was carefully analyzed. In this system, each signal path passes through a high-input-impedance buffer followed by a fourth-order Sallen-Key low-pass filter. This structure is intended to suppress high-frequency noise while preserving signal integrity.

The theoretical cutoff frequency f_c of a second-order Sallen-Key low-pass filter is given by:

$$f_c = \frac{1}{2\pi\sqrt{R_1 R_2 C_1 C_2}} \approx 194\,\text{Hz}$$

where R_1 and R_2 correspond to resistors **R84** and **R85** in the first Sallen–Key stage (each 820 kΩ), while C_1 and C_2 correspond to capacitors **C63** and **C65** (each 1 nF) shown in Fig. 3.2. These components form the first second-order low-pass stage, and two identical stages are cascaded to realize the overall fourth-order low-pass filter.

However based on LTspice simulation results, the -3 dB cutoff frequency was approximately 85 Hz. For a fourth-order Sallen–Key low-pass filter with Butterworth response, the equivalent noise bandwidth (ENBW) is approximately 1.1–1.2 times the cutoff frequency[56]:

$$\text{ENBW} \approx 1.1 \times 85 = 93.5\,\text{Hz}$$

Thermal (Johnson–Nyquist) noise from resistors is the dominant noise source in this path. For each 820 kΩ resistor, the thermal noise is calculated by:

$$V_{\text{thermal}} = \sqrt{4kTRB}$$

where k is the Boltzmann constant (1.38×10^{-23} J/K), T is the absolute temperature (here $T = 300\,\text{K}$), R is the resistance in ohms (each 820 kΩ), and B is the equivalent noise bandwidth (ENBW) of the signal path (here $B = 93.5\,\text{Hz}$).

The total thermal noise (RMS sum) is given by:

$$V_{\text{thermal, total}} = \sqrt{V_{\text{thermal, R1}}^2 + V_{\text{thermal, R2}}^2 + V_{\text{thermal, R3}}^2 + V_{\text{thermal, R4}}^2} \tag{3.1}$$

Therefore, for four equal resistors, the total thermal noise is:

$$V_{\text{thermal total}} = \sqrt{4 \times (1.269\,\mu\text{V})^2} \approx 2.253\,\mu\text{V}$$

In addition, the noise contribution of the operational amplifier is calculated based on a typical voltage noise density of $8\,\text{nV}/\sqrt{\text{Hz}}$ and three active stages:

$$V_{\text{opamp}} = 3 \times 8\,\text{nV}/\sqrt{\text{Hz}} \times \sqrt{93.5\,\text{Hz}} \approx 232\,\text{nV}$$

Current noise is negligible and can be ignored. Combining the noise sources using RMS summation:

$$V_{\text{total}} = \sqrt{(2.253\,\mu\text{V})^2 + (0.232\,\mu\text{V})^2} \approx 2.264\,\mu\text{V}$$

After considering both signal paths (working and reference electrode), and a gain of 10 in the differential amplifier, the output noise becomes:

$$V_{\text{output noise}} = 2.264\,\mu\text{V} \times 2 \times 10 = 45.28\,\mu\text{V}$$

LTspice simulation showed a very similar result of 48.571 (see Appendix A.1), indicating the hand calculation is reasonably accurate. The corresponding input-referred noise is:

$$V_{\text{in referred}} = \frac{48.571\,\mu\text{V}}{10} = 4.857\,\mu\text{V}$$

Comparison with ADC Resolution:

The ADC used is 12-bit with a full-scale input of 3.3 V. Therefore, the least significant bit (LSB) is:

$$\text{LSB} = \frac{3.3\,\text{V}}{2^{12}} = 805.7\,\mu\text{V}$$

Since the signal is amplified by 10, the input-referred LSB is:

$$\frac{805.7\,\mu\text{V}}{10} = 80.57\,\mu\text{V}$$

To maintain stable resolution, the total input-referred RMS noise should generally be less than 1/10 of the LSB:

$$\text{Allowed noise} = \frac{80.57\,\mu\text{V}}{10} = 8.06\,\mu\text{V}$$

The calculated noise of 4.857 µV is well below the required limit, showing that the designed analog front end and filters provide enough noise performance to support reliable ADC operation with 0.1 mV resolution.

3.2.4. Power management for AD8237

The AD8237 instrumentation amplifier is a key component in the front-end signal chain, and its supply configuration directly constrains both input and output voltage ranges. According to the datasheet, the device can operate from a single 1.8–5.5 V supply or from dual rails up to a maximum difference of 6 V. In practical design, the supply voltages must be chosen so that the amplified output stays well within the rails and avoids nonlinear behavior near the supply limits.

In this design, the input signal from the ISE electrodes spans 80–300 mV. With the selected gain of 10, the output is expected to range from about 0.8 to 3.0 V. The reference pin is tied to ground, so both input and output voltages are centered around 0 V. Although the AD8237 supports rail-to-rail operation, some margin must be kept, as signals that approach the rails may cause distortion or clipping. To provide enough margin, a dual-supply setup is used, with +4 V for the positive rail and –1.8 V for the negative rail. This power configuration offers several advantages. The total supply voltage of 5.8 V stays within the 6 V maximum limit, while the output swing from 0.8 V to 3.1 V remains safely inside the rails, preventing saturation. The small negative rail also keeps the low-level inputs away from the nonlinear region near ground. In addition, referencing REF to 0 V is supported directly without introducing offset errors.

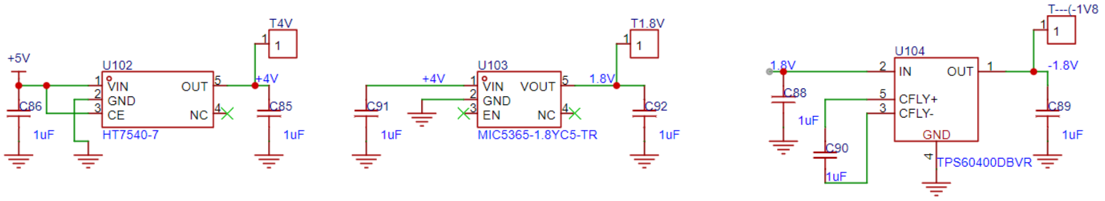

Figure 3.3: Power management architecture generating +4 V, +1.8 V and –1.8 V rails from a single +5 V input.

To generate the required supply rails from a single +5 V input, a compact three-stage power management circuit is used (Figure 3.3). First, a low-noise LDO regulator provides a stable +4 V analog supply from the +5 V system input. Then, a second LDO generates a clean +1.8 V rail, which drives a charge-pump inverter (TPS60400) to produce –1.8 V. Decoupling capacitors are added to reduce ripple and keep the negative output stable. In summary, this multi-stage regulation design provides +4 V and –1.8 V supplies suitable for the operating range of the AD8237.

3.3. Iontophoresis Voltage-Controlled Current Source Design

3.3.1. Design Principle

The core requirement of iontophoresis is to generate a stable and precisely controlled DC current between electrodes, enabling ions to penetrate skin barriers and reach target sweat glands. The circuit design in this work is inspired by, and largely follows, the voltage-controlled current source architecture proposed by Emaminejad et al. [11], as already mentioned in the review section (Fig. 2.3). Building on this foundation, the design here is adapted for sweat stimulation, with a target current range of 0–1.5 mA, real-time current monitoring, and additional safety features to ensure stable and reliable operation. The implemented circuit is shown in Fig. 3.4.

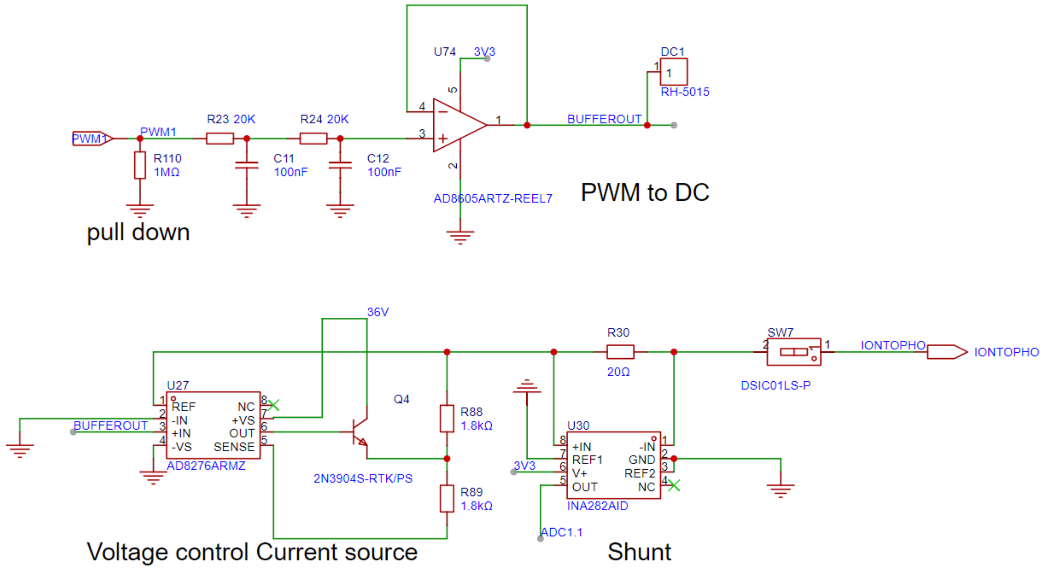

Figure 3.4: PWM filter and voltage-controlled current source

The current generation is achieved using a voltage-controlled current source architecture. First, a pulse-width modulation (PWM) signal is generated by the microcontroller. Pulse Width Modulation (PWM) is a widely used technique for analog control through digital signals. It works by rapidly switching a signal between high and low voltage levels, and adjusting the fraction of time that the signal stays high within each cycle—this fraction is called the duty cycle[57]. Although PWM signals are digital, with only two voltage levels, they can act as analog voltages after passing through a low-pass filter. The filter removes the high-frequency parts and produces a smooth average voltage.

The resulting DC voltage V_{dc} after filtering is directly proportional to the duty cycle and the supply voltage V_{supply}. The relationship can be expressed as:

$$V_{\mathrm{dc}} = \text{Duty Cycle} \times V_{\mathrm{supply}}$$

By varying the duty cycle, one can obtain any desired voltage level between 0 V and V_{supply}, making PWM a highly efficient and flexible method for voltage control.

By adjusting the duty cycle of the PWM output, we control the average voltage level of the signal. However, since PWM is a pulsed digital waveform, it must be converted into a smooth DC signal for analog control[58]. To achieve this, we apply a first-order RC low-pass filter composed of resistors and capacitors, which attenuates high- components and produces a stable output voltage V_{dc}.

To prevent loading effects and improve drive strength, the filtered signal is buffered using an AD8605 low-noise rail-to-rail operational amplifier. The buffered V_{dc} is then fed into a voltage-controlled current source composed of a differential amplifier (AD8276) and an NPN transistor (2N3904). The AD8276 precisely regulates the transistor's base voltage, allowing the transistor to operate in its active region, thus enabling a stable and linear current output. The resulting output current I_{out} is linearly dependent on the input control voltage and is given by:

$$I_{\text{out}} = V_{\text{dc}} \times 0.47\,\text{mA}/\text{V}$$

The conversion factor of 0.47 mA/V is defined by the resistor values and transistor characteristics in the current driver. This design offers high accuracy and good linearity in current control. For safety and flexibility, a single-pole single-throw (SPST) switch is placed in series with the output, so the current can be turned off during a fault or when it is not needed.

To enable real-time monitoring of the current, a precision shunt resistor (20 Ω) is placed in series with the output. According to Ohm's law, the voltage drop across this resistor is directly proportional to the current. This voltage is amplified by an instrumentation amplifier (INA328) and fed into an ADC for continuous current sensing. The value of the shunt resistor is chosen to balance between sufficient voltage swing for accurate ADC sampling and not exceeding the ADC input range at the maximum current of 1.5 mA.

3.3.2. Simulation Verification

To validate the performance and reliability of the iontophoresis module, we carried out two key simulations using Proteus software. These simulations focused on verifying the constant current source's stability under varying skin resistances and evaluating the linear controllability of the output current via PWM duty cycle adjustment.

We built the complete iontophoresis circuit model in Proteus, with the output path connected to a variable load resistor representing the equivalent skin impedance. Based on literature values, human skin impedance typically ranges from 5 kΩ to 13 kΩ, depending on factors like hydration, contact quality, and skin type. In the simulation, we swept the skin resistance within this range and observed the output current.

The result demonstrates that the output current remains constant even when the skin resistance changes, as long as the input control voltage (V_{dc}) is fixed. For example, with $V_{dc} \approx 2.85$ V, the output current stays at approximately 1.34 mA across the resistance range. This confirms that the voltage-controlled current source (VCCS) based on the AD8276 and 2N3904 maintains good load regulation and is capable of operating under high skin impedance conditions. The maximum supported resistance is determined by the system's power rail (36 V, circuit see Fig. 3.9), which theoretically allows up to 20 kΩ load under 1.5 mA current output.

Next, we simulated the linear controllability of the output current with respect to the PWM duty cycle. By sweeping the duty cycle from 0% to 100%, we obtained different V_{dc} values from the low-pass filter (see previous subsection), and recorded the corresponding output current. The result is shown in Fig. 3.5, where the relationship between PWM duty cycle and current is nearly linear.

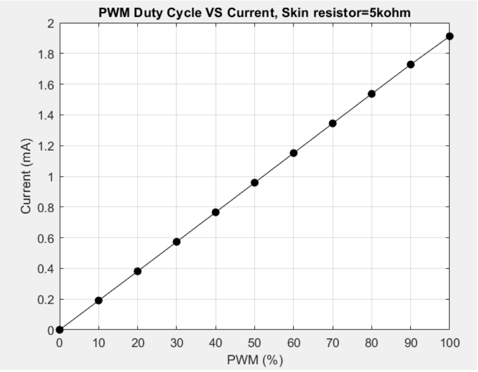

Figure 3.5: PWM duty cycle versus output current simulation.

This confirms that the system supports fine and linear programmable control over current output via PWM configuration, enabling precise adjustment in real applications.

3.4. Impedance Measurement Circuit

3.4.1. AD5933 Functional Diagram Overview

In this system, the sweat secretion rate is indirectly estimated by measuring impedance with the AD5933 (Analog Devices). The chip includes an AC excitation source, a 12-bit ADC, and a built-in discrete Fourier transform (DFT) engine[59]. This integration removes the need for external waveform generators or lock-in amplifiers, making the AD5933 suitable for low-power and portable sensing systems. The target impedance range of this design is 10–100 k, which reflects changes in sweat volume and ionic conductivity.

As shown in Figure 3.8, the device generates a sinusoidal excitation via its direct digital synthesis (DDS) engine. The signal passes through the unknown impedance $Z(\omega)$, is converted into voltage by a feedback resistor R_{FB}, and then conditioned by an on-chip PGA and low-pass filter before digitization. A 1024-point DFT extracts both real and imaginary components of the response, which are communicated to the MCU over I^2C.

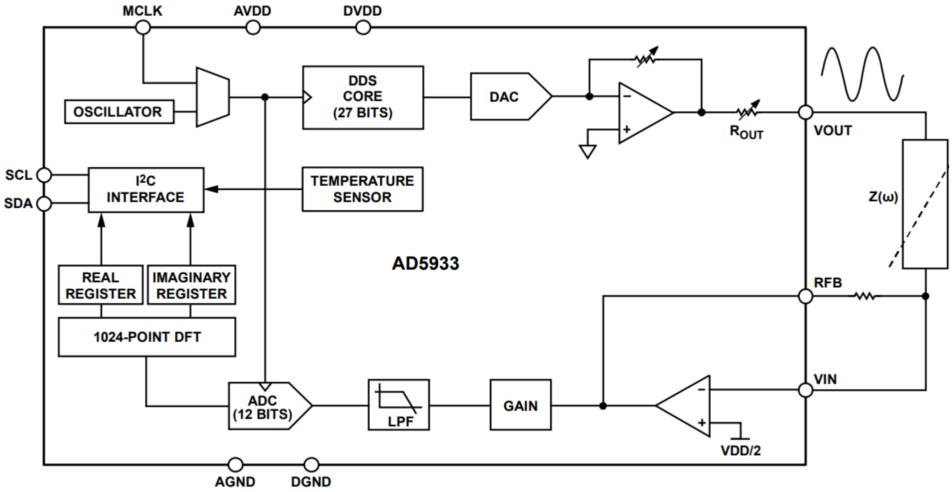

Figure 3.6: Functional block diagram of the AD5933 impedance measurement chip.[59]

3.4.2. Measurement Circuit Design and Calibration

For small impedances, direct excitation can cause electrode polarization or nonlinear distortion due to high current[59]. To solve these problems (Figure 3.7), two protection stages are added to the design. First, AC coupling capacitors with a bias network keep the DUT at mid-supply ($V_{\text{DD}}/2$), preventing DC offset build-up and maintaining symmetrical operation. Second, buffer amplifiers are placed between the DUT and the AD5933 to separate the excitation source from the measurement path, reducing loading effects and keeping the signal stable.

To convert raw complex outputs into real impedance values, calibration with known resistors is required. On the PCB, switchable calibration resistors (e.g., 1 kΩ, 10 kΩ) can be inserted into the measurement path. From the real and imaginary values obtained, a gain factor G is computed as:

$$G = \frac{1}{Z_{cal} \cdot \sqrt{Re^2 + Im^2}}. \tag{3.2}$$

This gain factor is then applied to subsequent measurements for accurate impedance estimation.

3.4.3. Dual-Path Measurement Strategy

A single-path design cannot cover both low and high impedances effectively. Therefore, a dual-path front-end is implemented:

- **Low-impedance path** (1 kΩ–10 kΩ): low excitation amplitude, AC coupling, and buffering to avoid polarization.

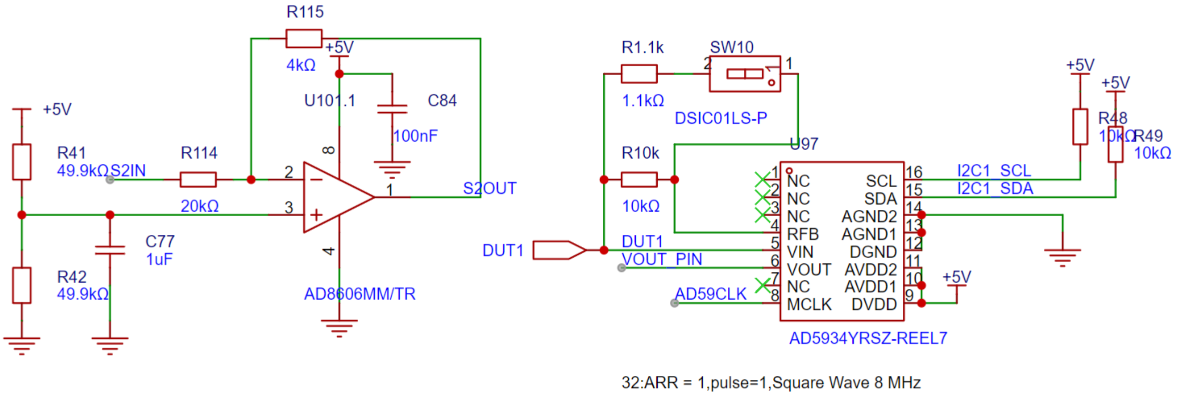

Figure 3.7: Small impedance measurement circuit with AC coupling and buffering.

- **Medium-to-high impedance path** (10 kΩ–100 kΩ): higher excitation amplitude for improved signal-to-noise ratio.

A digitally controlled multiplexer allows the MCU to switch between these two paths, enabling wide-range impedance measurement on the same platform.

3.5. MCU Integration

The microcontroller used in this system is the STM32F103C8T6, a 32-bit ARM Cortex-M3 MCU from STMicroelectronics. It was selected for its rich on-chip peripherals, which meet the project requirements for data acquisition, communication, and control. In particular, the STM32F103C8T6 includes a high-precision ADC, I^{2}C, and UART, allowing efficient sweat signal sampling and reliable data transfer[60].

Pin configuration and peripheral initialization were carried out using ST's graphical tool, STM32CubeIDE. This environment provides an easy-to-use interface for setting each pin's function, which greatly reduces setup errors compared with manual configuration. It also generates initialization code that is directly compatible with STM32CubeIDE.

To verify the MCU's basic functions, tests were carried out on a minimal development board, which is one of the most commonly used options for initial testing. First, an LED blink test confirmed proper GPIO output operation. Next, UART communication was checked using a terminal emulator to confirm stable data transmission and reception. Finally, ADC sampling and PWM output tests verified accurate analog input readings and stable PWM signal generation. These tests demonstrated the STM32F103C8T6's reliable performance and provided a solid foundation for full system integration.

3.6. Power management Circuit Design

Our system is powered by a single-cell 3.7 V lithium-ion battery. Since different modules require different voltage rails, a combination of boost converters and a low-dropout regulator (LDO) is adopted. Boost converters and LDOs are complementary in power management. Boost converters use high-frequency switching to step up voltage with high efficiency (80–95%)[61], making them suitable for generating 5 V and 36 V rails from the 3.7 V battery. However, the switching action introduces ripple and electromagnetic interference (EMI), which may affect sensitive analog circuits[62]. In contrast, LDOs operate by linear regulation, offering lower efficiency but excellent noise suppression and clean output[63]. Therefore, the whole system adopts boost converters for high-voltage generation and an LDO for the 3.3 V digital and analog supply, achieving a balance between efficiency and signal integrity.

High-Voltage Boost (3.7 V → 36 V) To maintain iontophoresis currents up to 1.5 mA across skin impedances as high as 20 kΩ, the system requires a high compliance voltage. A MAX5026EUT+T boost converter is selected to generate 36 V from the 3.7 V battery. A 47 μH inductor and a Schottky diode

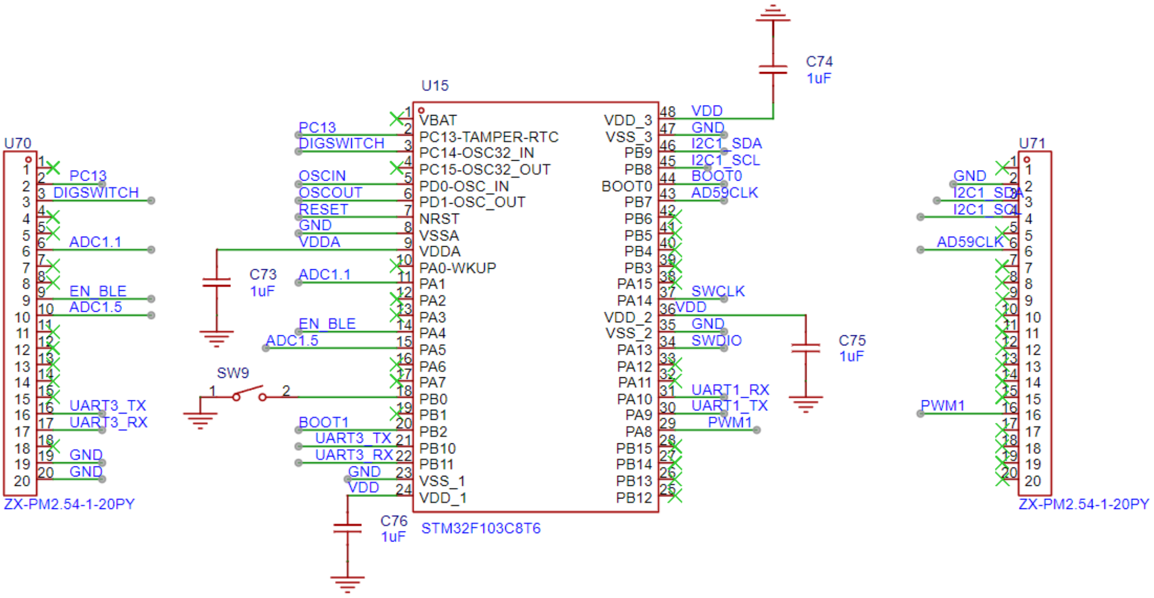

Figure 3.8: STM32F103C8T6 circuit design.

provide switching energy transfer, while feedback resistors (150 kΩ / 6.34 kΩ) set the output voltage. A 1 μF ceramic capacitor stabilizes the output.

Intermediate Boost (3.7 V → 5 V) To supply analog front-ends and act as an intermediate rail, the MT3608 boost converter is used to step up the battery voltage to 5 V. A 10 μH inductor provides energy storage, a Schottky diode ensures fast switching with low loss, and feedback resistors (75 kΩ / 10 kΩ) regulate the output. Input and output capacitors (22 μF) reduce ripple and improve transient stability.

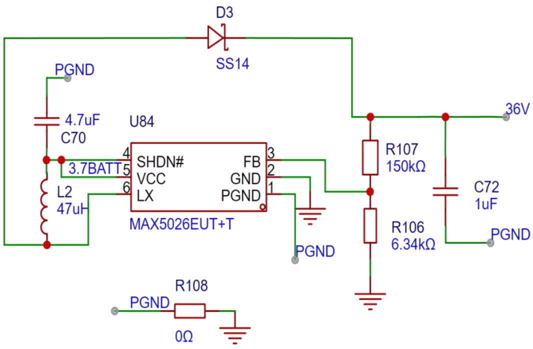

Figure 3.9: Boost converter circuit generating 36 V for iontophoresis.

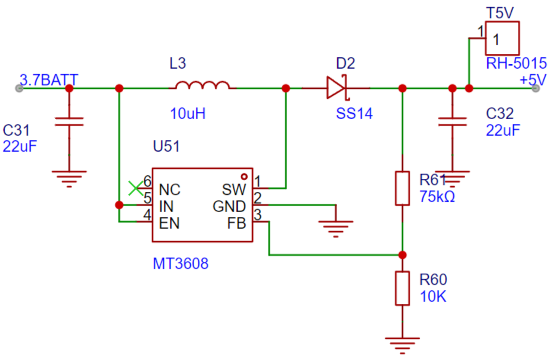

Figure 3.10: Boost converter circuit generating 5 V from the 3.7 V battery.

Low-Dropout Regulator (5 V → 3.3 V) The STM32 MCU, BLE module, and digital logic require a stable 3.3 V rail. An AMS1117-3.3 LDO is selected for its low output noise and strong ripple rejection, which are critical for precise ADC sampling and reliable communication. A combination of electrolytic and ceramic capacitors (47 μF and 100 nF) provides input decoupling and output stability.

4

PCB Layout Design and Firmware

4.1. PCB Layout Strategies

4.1.1. PCB Layout Overview

The first prototype PCB was designed as a test platform to validate circuit functionality rather than as a final miniaturized flexible board. The board size is 7 cm × 9 cm, which provides enough space for soldering, debugging, and clear placement of test points and connectors (Figure 4.1).

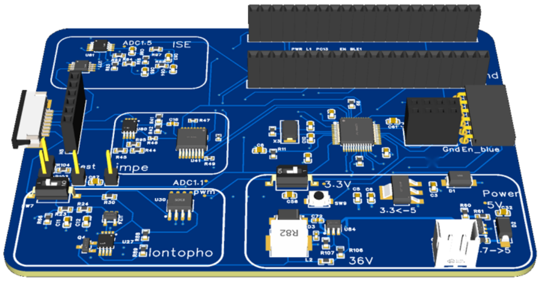

Figure 4.1: 3D model of the first prototype PCB.

To ensure reliable operation in a mixed-signal environment, the layout was divided into several functional zones (Figure 4.2). The left side hosts the analog front-end, including the ion-selective electrode (ISE) readout, iontophoresis driver, and impedance measurement circuits. These blocks are placed close together to shorten sensitive signal paths and reduce noise pickup. The right side is reserved for digital circuits, such as the microcontroller, communication interfaces, and indicator LEDs, which are isolated from the analog section to minimize interference. Power management modules are located near the boundary, providing stable supply rails to both domains.

4.1.2. Grounding Strategy

In mixed-signal PCB design, the ground plane layout is very important because it directly affects signal return paths, noise coupling, and overall electromagnetic compatibility[64]. At first, we compared two grounding methods: the "star grounding" and the "full copper pour." The star grounding method connects each module's ground trace to a single point, which in theory separates analog and digital grounds to reduce crosstalk. In practice, however, this approach creates long return paths that spread out from the center, increasing loop area and adding unwanted inductance and coupling. These effects can lower signal integrity and worsen EMI performance[65].

In contrast, the full copper pour method uses a continuous ground plane that covers the entire PCB. This provides the shortest return path for all signals, simplifies routing, and improves ground connections between layers in multi-layer boards. However, this approach can couple high-frequency digital noise into nearby analog circuits, increasing the analog reference noise floor[64]. To reduce this effect, we

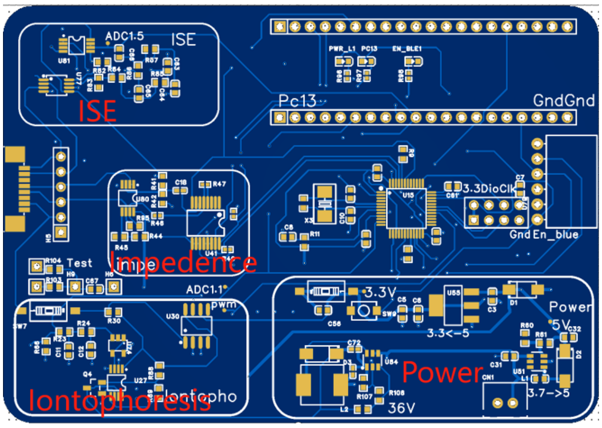

Figure 4.2: Functional partitioning of the PCB into analog and digital zones.

separated the analog and digital regions physically and added ground vias in key locations to limit crosstalk.

After comparing the trade-offs, we chose the full copper pour strategy. Once the ground plane was applied, vias was placed along the edges of every GND pin to avoid isolated copper regions. If routing changes are needed later, adjusting these vias can quickly keep ground continuity.

This ground design provides a low-impedance, low-noise return path for analog signals and a stable reference for digital circuits, greatly improves system stability and resistance to interference in a mixed-signal environment.

4.1.3. Signal Routing Principles

In this PCB design, the signal routing strategy plays a critical role in ensuring electromagnetic compatibility (EMC), signal integrity, and ease of debugging.

High-frequency and high-speed signals—including I^2C communication lines, ADC analog inputs, the Serial Wire Clock (SWCLK) programming interface, and crystal oscillator traces—were given the highest routing priority. These signals are especially sensitive to crosstalk, impedance changes, and loop-induced noise. To reduce these effects, the "3W rule" was applied, keeping at least three times the trace width of spacing between adjacent high-speed lines to minimize parasitic coupling and capacitive interference.

For analog signals, such as the ADC input channels, a perpendicular crossing strategy was adopted relative to high-speed or switching traces. This means analog lines intersect digital or power paths at right angles whenever possible, avoiding parallel alignment that could lead to electromagnetic interference.

4.1.4. Decoupling and Power Integrity

In designing the power supply layout for this PCB, care was taken to minimize switching noise and ensure stable voltage delivery to critical components. Basic layout practices such as minimizing high-frequency loop areas, placing decoupling capacitors close to IC power pins, and separating switching and analog regions—were applied to support stable operation and reduce potential interference.

Firstly, in the 3.7 V to 5 V boost converter section (Figure 4.3), the high-frequency switching loop area was minimized. This loop, formed by the switching node (SW), Schottky diode, inductor, and output capacitor, can be a major source of electromagnetic interference (EMI) if not well controlled. To reduce this effect, the components were placed as close as possible, with short copper traces forming a tight and efficient loop. Wide copper pours and multiple vias were also added at key points to strengthen the current return paths and improve EMI suppression.

Secondly, in the 36 V buck converter section, a similar design philosophy was applied. Components operating at high current and high voltage — such as inductors and diodes — were laid out in a compact manner with wide, short traces.Copper was intentionally kept away from the area under the inductors to prevent noise coupling into the ground plane. In addition, high-speed switching nodes were carefully kept out of the analog regions to avoid interference with sensitive ADC signal paths.For decoupling capacitor placement, a close-placement strategy was used. Each critical IC was paired with its corresponding decoupling capacitor located as close as possible to the power pins. The layout follows the shortest loop principle: VDD → Capacitor → GND, ensuring minimal impedance in the power loop. This design effectively reduces voltage ripple and keeps the supply rail stable. To further improve power integrity, wide copper traces were used along high-current paths, and multiple ground vias were added to connect ground layers vertically. This helps reduce voltage drop from resistive losses and improves heat dissipation.

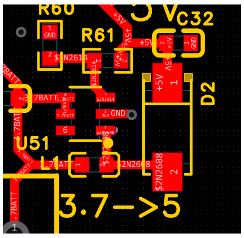

Figure 4.3: 3.7V to 5V boost circuit layout to reduce loop area

4.2. Firmware Architecture and working Principle

The entire system is controlled by the STM32 microcontroller, which performs three main functions: (i) collecting analog data from the sensing front end, (ii) controlling the iontophoresis and other peripheral modules, and (iii) sending data wirelessly through Bluetooth. Because this application runs only a few tasks and has clear timing requirements, using a full Real-Time Operating System (RTOS) would add extra timing management and complexity without real benefits. Instead, the firmware uses a simple structure based on timer interrupts and Direct Memory Access (DMA). All time-critical tasks, such as periodic sampling, data buffering, and communication, are handled inside interrupt service routines (ISRs), which keeps the timing stable and reduces jitter.

4.2.1. Data Acquisition and Control

This system uses an STM32 microcontroller to continuously read analog signals. It uses the built-in 12-bit SAR ADC together with Direct Memory Access (DMA). This setup allows stable and fast sampling of low-frequency biosignals, while reducing CPU workload.

The SAR ADC works by comparing the input voltage step by step, and it finishes each conversion in a few microseconds. It provides a good balance between speed and accuracy, which is suitable for biomedical signals. In STM32CubeMX, multiple ADC channels are enabled with different sampling times. This allows the system to read signals from the ion-selective electrode, impedance path, and other analog sources at the same time, without making the firmware too complex.

To reduce CPU usage, DMA is set up to move ADC data directly into a memory buffer. This avoids the need for the CPU to check ADC values all the time. When DMA finishes one round of transfer, it sends an interrupt to the firmware. Both the ADC and DMA work in circular mode, so the memory keeps updating automatically. This helps the system collect data smoothly and continuously for real-time use.

To drive the iontophoresis circuit, the firmware uses a timer on the STM32 microcontroller to generate a PWM signal. The principle of PWM duty cycle adjustment and low-pass filtering is explained in subsection 3.3.1. In the firmware, the PWM frequency is set in the kilohertz range. This helps deliver a smooth current and avoids audible noise. The timer prescaler and auto-reload values are chosen to keep a good balance between frequency resolution, timing accuracy, and CPU load. The timer output frequency is calculated as:

$$f = \frac{f_{\text{clk}}}{(\text{PSC} + 1) \times (\text{ARR} + 1)}$$

where f_{clk} is the timer input clock frequency, PSC is the prescaler value, and ARR is the auto-reload value.

The following parameters were used in this work as a practical reference for system implementation: $f_{\text{clk}} = 72\,\text{MHz}$, $PSC = 71$, and $ARR = 999$. With these settings, the resulting timer frequency is:

$$f = \frac{72\,\text{MHz}}{(71 + 1) \times (999 + 1)} = 1\,\text{kHz}.$$

During operation, the duty cycle is changed through the Capture/Compare Register (CCR). This lets the firmware adjust the stimulation current in real time.

4.2.2. Wireless communication and Data package

In this system, Bluetooth Low Energy (BLE) wireless communication is implemented via a UART-connected module (HC-05) to transmit both ADC-acquired analog signals and impedance measurement results to an external host device. A hardware timer on the STM32 microcontroller is set to trigger an interrupt every few seconds. When the interrupt occurs, the firmware starts one full data collection cycle. It reads the analog voltages from the ADC buffer (filled by DMA) and starts an impedance measurement using the AD5933 chip through the I²C interface. After the real and imaginary parts of the impedance are read, all the data are processed and combined into a structured data packet. Each data packet includes a fixed header, an optional timestamp, ADC voltage readings, and the complex impedance result. These elements are converted into a byte stream and sent to the BLE module through UART. The UART is set for asynchronous communication at 115200 baud, with 8 data bits, 1 stop bit, and no parity. To reduce CPU load, UART transmission works in non-blocking mode. The HC-05 module operates in transparent serial mode, sending the UART byte stream over BLE without the need for AT command parsing or extra runtime settings. Once powered on and paired with a mobile device, all UART data can be sent wirelessly.

5

Results and Discussion

5.1. Functional verification of subsystems

5.1.1. Validation of main control unit and Power management

The main control unit is the center of the system and manages signal collection, data processing, and wireless communication. Testing this part was important to make sure the whole prototype could work as designed. The test started with a simple power-on check. When 3.3 V was applied to the board, the power indicator LED turned on right away, showing that the MCU and its related circuits were powered correctly.

Subsequently, the programming interface was evaluated using the ST-LINK programmer. The MCU was successfully detected by the STM32CubeIDE environment, and a simple test program was uploaded without error (Fig. 5.1). Step-by-step debugging confirmed proper initialization of the system clock and memory. To verify the communication interfaces, the UART module was tested by transmitting strings to a serial terminal. The messages appeared correctly on the host PC, demonstrating that the peripheral and software drivers were functional. In addition, the Bluetooth module (HC-05) was paired with a laptop. When the Bluetooth module changes from flashing quickly to flashing once every four seconds, it means that the pairing is successful. The data transmitted from the Bluetooth module was received on a PC using the SSCOM serial communication software, confirming stable wireless communication (Fig. 5.2). For testing power management, a multimeter was used in DC mode, and the voltage range

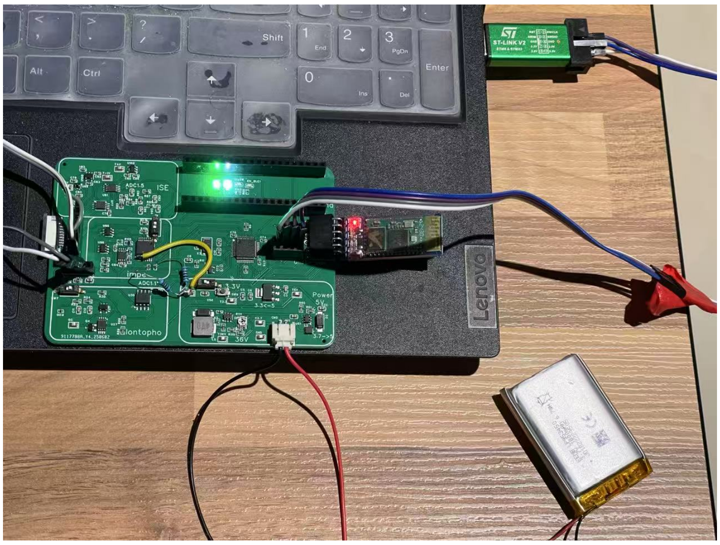

Figure 5.1: MCU power-on test, burning test and Bluetooth test

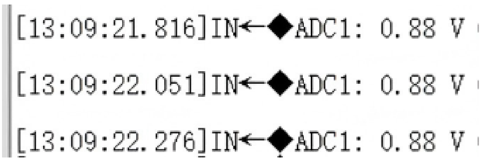

```
[13:09:21.816]IN←◆ADC1: 0.88 V
[13:09:22.051]IN←◆ADC1: 0.88 V
[13:09:22.276]IN←◆ADC1: 0.88 V
```

Figure 5.2: Bluetooth transmission interface in SSCOM

was selected according to the expected value. We first tested the boost converter from 3.7 V to 36 V. The multimeter was set to the 200 V range, and the output voltage was measured while adjusting the potentiometer with a small screwdriver. The output voltage could be smoothly adjusted from 24 V to 36 V as expected. Next, the 3.7 V to 5 V boost converter was tested. It provided a stable 5 V output. Also, the AMS1117 LDO correctly converted the 5 V rail into 3.3 V for the MCU and other low-voltage analog parts. The converters maintained the expected voltage levels over the full input range, ensuring stable operation of the following functional modules, such as the iontophoresis circuit and the impedance measurement block.

Overall, the basic verification results show that the fundamental functions of the system work properly as designed. The main control unit can start up reliably, run the program, and support both serial and wireless communication. The power management part also worked as expected. The measured outputs of 5 V, 3.3 V, and up to 24 V remained stable under different input conditions, confirming the proper function of the boost converter and voltage regulation stages.

5.1.2. Iontophoresis circuit testing

The iontophoresis circuit is responsible for generating a controlled microcurrent that enables sweat induction through the skin. The validation was performed in three stages. First, the microcontroller was programmed to generate a 1 kHz PWM signal with a 50% duty cycle. The waveform was measured on an oscilloscope (Fig. 5.3) , and the result confirmed a stable square wave with the expected frequency and duty ratio. Second, the PWM signal was passed through a low-pass filter to obtain a DC control voltage. The voltage was measured using a digital multimeter, showing 1.657 V (Fig. 5.4). This value is consistent with the theoretical expectation of $3.3 \times 50\% = 1.65$ V, demonstrating correct functionality of the filtering stage. Finally, the circuit was evaluated under load conditions. With a 10 kΩ resistor connected, the voltage-controlled current source produced a stable output current of approximately 0.88 mA. The current value was measured both with a multimeter and transmitted via the Bluetooth module to the host PC, where it was displayed correctly. This confirmed that the system is capable of delivering and monitoring microcurrents in real time.

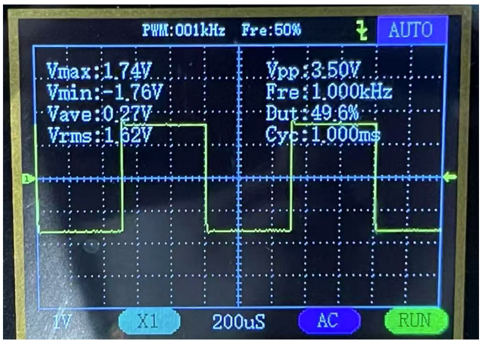

Figure 5.3: PWM in oscilloscope, 1 kHz

Setpoint accuracy across duty cycles

To check how well the output matched the programmed duty cycle, the PWM signal was set to different values from 10% to 90%. The filtered DC voltage was measured using a standard handheld multimeter (XJIE XJ-9205S, nominal accuracy ±0.5% + 2 digits), and the output current will cross a 10 kΩ load and recorded by shunt and ADC .The theoretical output current (I_{exp}) was obtained from the designed transconductance ratio of 0.47 mA/V. Meanwhile, the measured current (I_{ADC}) was derived from the

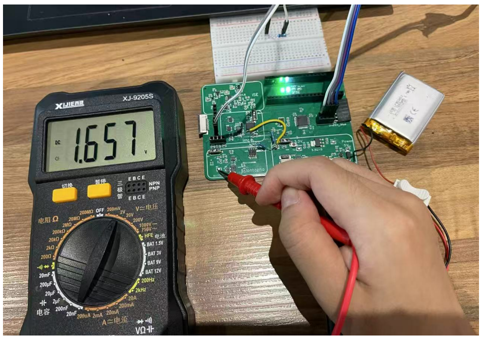

Figure 5.4: Measuring the DC voltage by multimeter

ADC voltage readings, which correspond to the voltage across a shunt resistor.The ADC operated at 12-bit resolution with a 3.3 V reference. Table 5.1 shows that the measured voltages and currents were very close to the theoretical values.

Table 5.1: Setpoint accuracy and corresponding measured current

D (%)	V_{exp} (V)	V_{meas} (V)	I_{exp} (mA)	I_{ADC} (mA)
10	0.33	0.331	0.156	0.139
20	0.66	0.664	0.312	0.311
30	0.99	0.994	0.467	0.494
40	1.32	1.326	0.623	0.683
50	1.65	1.657	0.777	0.869
60	1.98	1.988	0.934	1.058
70	2.31	2.310	1.086	1.246
80	2.64	2.640	1.241	1.436
90	2.97	2.970	1.396	1.623

Measured voltages were obtained using a handheld multimeter (XJIE XJ-9205S, accuracy ±0.5% + 2 digits, corresponding to approximately ±10 mV uncertainty). I_{ADC} values were obtained by averaging a sequence of ADC readings over several seconds to suppress random noise.

Compliance range with different loads

The compliance of the current source was assessed by maintaining a fixed PWM duty cycle and varying the load resistance from 5 kΩ to 20 kΩ. For each load, the ADC-measured current (I_{ADC}) was obtained from the voltage ADC reading across the shunt resistor. As shown in Table **??**, the measured current remained nearly constant at approximately 1 mA across different load resistances, showing the stable compliance performance of the voltage-controlled current source.

Table 5.2: Compliance test of the voltage-controlled current source at $D = 60\%$

D (%)	R_{load} (kΩ)	I_{ADC} (mA)
60	5.1	1.0578
60	6.8	1.0568
60	10.0	1.0575
60	11.9	1.0569
60	15.1	1.0583
60	20.0	1.0571

5.2. Experimental challenges and limitations

5.2.1. Ion-selective electrode (ISE) module analysis

The ISE readout module was tested by enabling the MCU ADC interface and monitoring the amplified electrode signals. In the first tests, the ADC correctly read values under firmware control. This confirmed that the digital interface was working. However, when a differential input of about 0.2 V was applied to the instrumentation amplifier, the output voltage was very small. This did not match the expected amplification.

To find the cause, the supply rails of the amplifier were measured. The positive supply was correct at +4 V. But the negative rail, which should provide –1 V, was at 0 V. Further checks showed that the charge pump, which generates the negative voltage, was at fault. Although its 1 V input was present, the device failed to produce the required –1 V output.

Interpretation of Results:Supply and Reference Issues
The initial evaluation of the ISE readout module revealed two major causes for the observed malfunction. The first issue was traced to the negative supply generation. The charge pump, intended to generate –1 V, consistently failed and instead produced 0 V. A closer review of the datasheet indicated that the device requires a minimum input of 1.6 V to operate correctly, whereas in the prototype only 1.0 V was provided. As a result, the charge pump could not generate the intended negative rail and defaulted to ground.

A second critical error was identified in the schematic: the R_{FB} pin of the instrumentation amplifier had been incorrectly connected as the V_{out} node to the subsequent stage. This misconnection caused the amplifier to output a very low and invalid signal. Because this error was embedded in the schematic, it could not be corrected through rework or soldering. This highlighted the consequences of insufficient schematic verification and motivated immediate corrections in the second revision of the PCB design.

To resolve the first issue, the power supply strategy was simplified in the revised design. Instead of generating 4 V from 5 V and subsequently regulating to 1 V before inverting, the new approach directly uses the 3.7 V battery input, regulates it to 1.8 V, and then applies the charge pump to produce –1.8 V. This configuration not only satisfies the input requirements of the charge pump but also provides a dual supply of 3.7 V and –1.8 V (a total swing of 5.5 V), which meets the operating range of the instrumentation amplifier while reducing circuit complexity. The new schematic of readout path circuit is shown in Fig. 5.5. Finally, the supply voltage of the filter stage was reconsidered. Since the output of the filter is directly connected to the MCU ADC, whose reference is 3.3 V, powering the filter at higher voltages risked saturating the ADC input. Therefore, the filter supply was modified to 3.3 V to ensure compatibility with the ADC input range and to prevent overrange conditions.

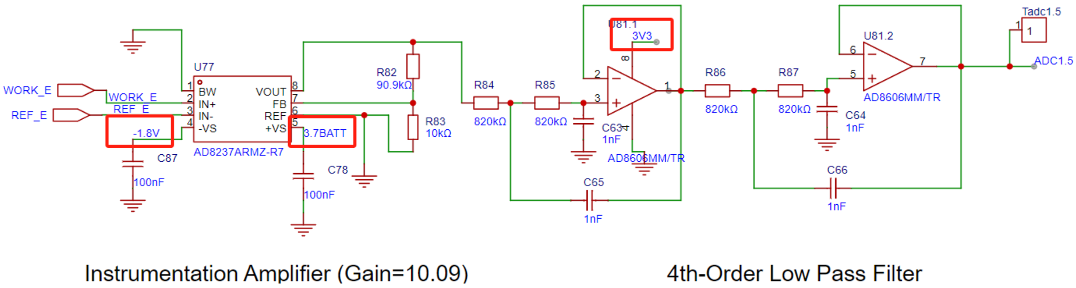

Figure 5.5: The modified schematic of ISE

5.2.2. AD5933 sweat rate impedance measurement

The impedance measurement functionality of the AD5933 was extensively evaluated. In the initial configuration, the device was connected following the recommended schematic, with R_{FB} and the device-under-test (DUT) both set to 10 kΩ. The control registers were programmed through I^2C to configure the excitation frequency, initialize the sweep, and subsequently poll the status register until valid real and imaginary values became available. However, the device failed to assert the data-valid flag as the fig5.6, and both real and imaginary registers remained unchanged. Based on discussions in user forums, it was suggested that the AD5933 requires a 3.3 V supply and 3.3 V I^2C pull-up resistors instead of 5 V. The board was modified accordingly through wire reworkA.2, but the issue persisted. Furthermore, oscilloscope measurements at the VOUT pin showed no sinusoidal output, even when the programmed excitation amplitude was increased to 2 V_{pp}.

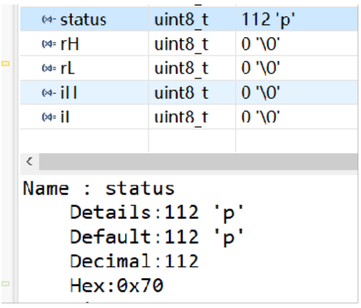

```
status    uint8_t    112 'p'
rH        uint8_t    0 '\0'
rL        uint8_t    0 '\0'
iH        uint8_t    0 '\0'
iL        uint8_t    0 '\0'

Name : status
    Details:112 'p'
    Default:112 'p'
    Decimal:112
    Hex:0x70
```

Figure 5.6: The status register fail to valid

To verify that the problem was not caused by a faulty chip, an evaluation setup was created using a standalone AD5933 device (Fig. 5.7) with minimal connections (VDD = 3.3 V, GND, SCL, SDA) interfaced to an STM32 development board. In this simplified setup, the internal temperature register could be read and showed varying values, confirming that the I^2C interface was functional. When connected in a test loop using R_{LIM} and R_{CAL} referenced to ground, sinusoidal signals were successfully observed at both VOUT and VIN, demonstrating that the excitation circuitry was operational(Appendix A.3).

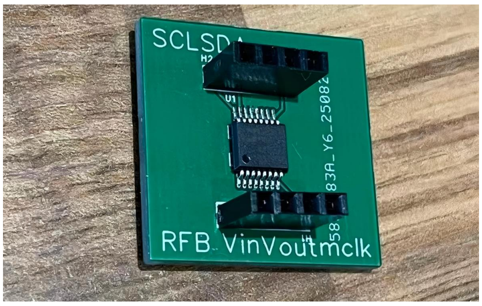

Figure 5.7: Single ad5933 chip adapter board

Following this, a calibration was performed with a known 10 kΩ resistor. The system produced a valid gain factor G, and subsequent impedance measurements of 5 kΩ and 20 kΩ resistors yielded correct results within the expected tolerance. These results confirm that the AD5933 can perform impedance measurements reliably when supplied and configured correctly. The failure observed in the integrated PCB prototype was therefore attributed to chip burnout or power-supply issues, which will be addressed in the next design iteration in the future.

6

Future Work and Conclusion

6.1. Future Work

6.1.1. Design Principles for Rigid–Flex Wearable PCBs

As mentioned in the background, polyimide (PI) is widely used as a substrate for flexible PCBs because of its high strength, good thermal stability, and compatibility with standard PCB manufacturing processes. While the background section focused on material choice, this part reviews the key mechanical layout strategies reported in the literature for building reliable rigid–flex PCB. These principles form the basis for the second-version design described in the following section.

One major consideration is the distribution of rigid and flexible regions. In wearable devices, heavy and bulky components such as chips, connectors, or batteries cannot be reliably mounted on fully flexible films. To address this, many designs adopt a "rigid island – flexible bridge" structure, where stiffened areas hold critical components and flexible sections connect them. This layout allows bending to occur mainly in the bridges while keeping the solder joints and pads stable on the rigid islands[40].

At the interface between rigid and flexible regions, stress concentration can occur. To reduce this effect, techniques such as teardrop pads, fillets, or gradual tapering of copper edges are commonly used[66]. In addition, stiffeners made of FR-4 or additional PI layers are often introduced beneath heavy components to reinforce solder joints and prevent delamination[37].

Trace routing also requires careful attention. Recommended practices include placing traces perpendicular to the bending axis, avoiding sharp corners, and using smooth curved paths. These measures help distribute strain evenly and reduce stress concentration[67]. Pads, vias, and other rigid features are generally kept away from high-strain hinge regions to avoid premature failure.

6.1.2. Flexible PCB V2 Layout and Mechanical Design

The second version of the PCB was redesigned to fix problems from Version 1 and to better support wearable use. Unused interfaces were removed to make the board simpler. Layout errors were also corrected to ensure normal operation. A top view of the basic layout is presented in Figure 6.1.

The new design was implemented on a flexible polyimide (PI) substrate, which provides the mechanical flexibility required for skin-mounted electronics. Components were also rearranged. Heavy and sensitive parts, such as the MCU and connectors, were placed in reinforced zones. In the flexible bridge, only straight traces were kept, without vias or sharp bends, to improve bending endurance and reduce the risk of copper fatigue. This follows the expected bending direction and reduces stress on solder joints. To show the regions more clearly, a 3D view of the PCB is provided in Figure 6.2.

A rigid–flex bridge structure was used in this design. The rigid "islands" carry the chips and larger passive components, while the middle section remains flexible to allow the board to bend. The substrate has a 25 μm PI core. On the bottom side, a 0.2 mm PI stiffener was added under the heavy parts. All surface-mounted components were placed on the top layer.For completeness, the back view with

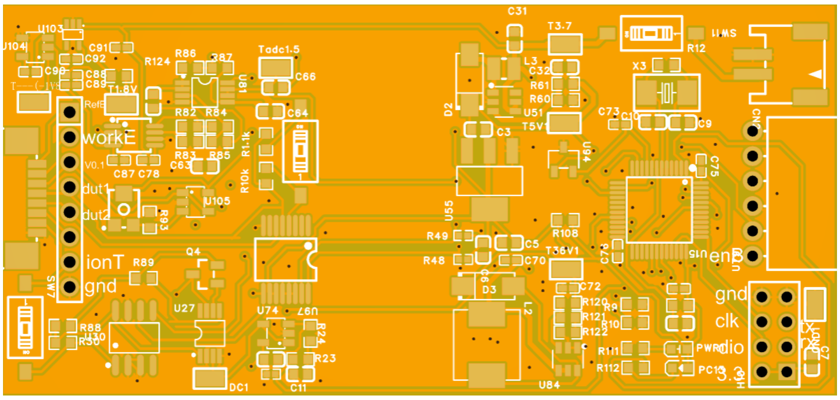

Figure 6.1: PCB Version 2 layout (top view).

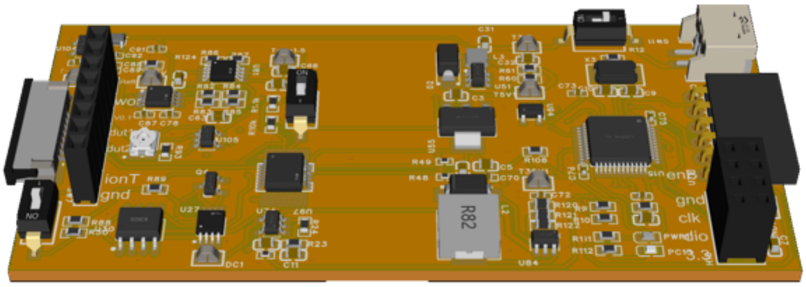

Figure 6.2: 3D view of PCB Version 2 showing rigid and flexible regions.

stiffeners is shown in Figure 6.3.

This structure has two main advantages:

- **Controlled stress distribution:** During bending, strain is concentrated in the flexible bridge. This prevents cracks or delamination near the reinforced edges.
- **Improved stability:** Rigid islands give strong support for chips and connectors. This avoids detachment and pad damage. At the same time, not using full-board stiffening keeps the design flexible and prevents random stress points.

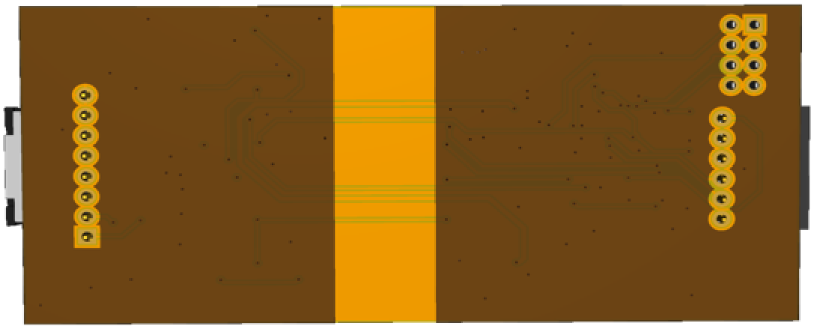

Figure 6.3: PCB Version 2 layout (back view with stiffeners).

In summary, the Version-2 PCB applies a hybrid rigid–flex structure. It allows the board to bend with the skin, while keeping important parts safe. Future work will include bending and fatigue tests to check long-term reliability.

6.2. Conclusion

This thesis has presented the conceptualisation, design, implementation, and evaluation of a flexible PCB-based readout system for wearable sweat sensing. The main goal was to develop an electronic platform capable of continuously and non-invasively acquiring and transmitting physiological information from human sweat. The work covered the entire development process, including backgound knowledge, circuit design, layout design, experimental validation, and iterative redesign.

The first version of the prototype (V1) successfully integrated several critical subsystems. The STM32-based main control unit was validated to support programming, debugging, and both serial and wireless (Bluetooth) communication, ensuring reliable data handling. The power management stage demonstrated robust performance across a wide input range (3.7–36 V), providing stable 5 V and 3.3 V rails for digital and analog blocks. The iontophoresis circuit was shown to generate controlled microcurrents from a PWM-derived voltage, with the resulting signals accurately measured and transmitted to a host PC, confirming the feasibility of sweat stimulation and monitoring within a wearable device.

Nevertheless, significant challenges were encountered. The ion-selective electrode (ISE) readout chain failed to deliver the expected amplification due to an incorrectly implemented negative supply and a schematic connection error that could not be corrected by rework. The AD5933-based impedance module also presented persistent issues on the integrated board, including the absence of excitation output and invalid register flags. Through independent testing on a standalone AD5933 adapter board, these functions were later verified to operate correctly.

Building on the lessons from V1, a second-version prototype (V2) was proposed with targeted improvements. By removing unused interfaces and optimizing component placement according to bending direction, the V2 layout is expected to perform more reliably under practical conditions. Looking ahead, the next steps involve the fabrication and testing of the V2 prototype. Comprehensive validation of impedance and electrolyte measurements under physiological conditions will be critical to demonstrate full system capability. Additional refinements, such as miniaturized wireless modules and integration with mobile applications, will further advance the system toward real-world deployment. Despite the limitations of the first version, the iterative design and experimental process have provided valuable insights into both the electronic and mechanical challenges of flexible biosensor platforms.

In conclusion, this thesis shows the feasibility of a wearable sweat-sensing system and highlights the step-by-step nature of hardware development, where each problem leads to a more robust redesign. The work provides a complete framework for flexible readout electronics, including analog signal acquisition, power management, micro-current control, wireless data transfer, and flexible PCB design. Overall, this work represents a small but meaningful step toward fully integrated and non-invasive sweat biosensors for personal health monitoring and wearable medical devices.

References

[1] Jihong Min et al. “Skin-Interfaced Wearable Sweat Sensors for Precision Medicine”. In: *Chemical Reviews* 123.8 (Apr. 2023). Publisher: American Chemical Society, pp. 5049–5138. ISSN: 0009-2665. DOI: `10.1021/acs.chemrev.2c00823`. URL: `https://doi.org/10.1021/acs.chemrev.2c00823` (visited on 09/25/2025).

[2] K. Wilke et al. “A short history of sweat gland biology”. en. In: *International Journal of Cosmetic Science* 29.3 (2007). _eprint: https://onlinelibrary.wiley.com/doi/pdf/10.1111/j.1467-2494.2007.00387.x, pp. 169–179. ISSN: 1468-2494. DOI: `10.1111/j.1467-2494.2007.00387.x`. URL: `https://onlinelibrary.wiley.com/doi/abs/10.1111/j.1467-2494.2007.00387.x` (visited on 08/31/2024).

[3] K. Sato, R. Leidal, and F. Sato. “Morphology and development of an apoeccrine sweat gland in human axillae”. In: *American Journal of Physiology-Regulatory, Integrative and Comparative Physiology* 252.1 (Jan. 1987). Publisher: American Physiological Society, R166–R180. ISSN: 0363-6119. DOI: `10.1152/ajpregu.1987.252.1.R166`. URL: `https://journals.physiology.org/doi/abs/10.1152/ajpregu.1987.252.1.R166` (visited on 08/31/2024).

[4] Jason Heikenfeld et al. “Accessing analytes in biofluids for peripheral biochemical monitoring”. en. In: *Nature Biotechnology* 37.4 (Apr. 2019). Publisher: Nature Publishing Group, pp. 407–419. ISSN: 1546-1696. DOI: `10.1038/s41587-019-0040-3`. URL: `https://www.nature.com/articles/s41587-019-0040-3` (visited on 05/30/2024).

[5] James Moyer et al. “Correlation Between Sweat Glucose and Blood Glucose in Subjects with Diabetes”. In: *Diabetes Technology & Therapeutics* 14.5 (May 2012). Publisher: Mary Ann Liebert, Inc., publishers, pp. 398–402. ISSN: 1520-9156. DOI: `10.1089/dia.2011.0262`. URL: `https://www.liebertpub.com/doi/full/10.1089/dia.2011.0262` (visited on 05/28/2024).

[6] Wei Gao et al. “Fully integrated wearable sensor arrays for multiplexed in situ perspiration analysis”. en. In: *Nature* 529.7587 (Jan. 2016). Publisher: Nature Publishing Group, pp. 509–514. ISSN: 1476-4687. DOI: `10.1038/nature16521`. URL: `https://www.nature.com/articles/nature16521` (visited on 06/17/2024).

[7] Douglas L. Bovell. “The evolution of eccrine sweat gland research towards developing a model for human sweat gland function”. en. In: *Experimental Dermatology* 27.5 (2018). _eprint: https://onlinelibrary.wiley.com/doi/pdf/10.1111/exd.13556, pp. 544–550. ISSN: 1600-0625. DOI: `10.1111/exd.13556`. URL: `https://onlinelibrary.wiley.com/doi/abs/10.1111/exd.13556` (visited on 08/31/2024).

[8] K. Sato et al. “Biology of sweat glands and their disorders. I. Normal sweat gland function”. In: *Journal of the American Academy of Dermatology* 20.4 (Apr. 1989), pp. 537–563. ISSN: 0190-9622. DOI: `10.1016/S0190-9622(89)70063-3`. URL: `https://www.sciencedirect.com/science/article/pii/S0190962289700633` (visited on 08/31/2024).

[9] Zhongzeng Zhou et al. “Autonomous Sweating Wearable Platform for Bilirubin Sensing Based on Thermal Stimulation”. In: *Analytical Chemistry* 96.51 (Dec. 2024). Publisher: American Chemical Society, pp. 20247–20254. ISSN: 0003-2700. DOI: `10.1021/acs.analchem.4c04592`. URL: `https://doi.org/10.1021/acs.analchem.4c04592` (visited on 09/25/2025).

[10] Minqiang Wang et al. “A wearable electrochemical biosensor for the monitoring of metabolites and nutrients”. en. In: *Nature Biomedical Engineering* 6.11 (Nov. 2022). Publisher: Nature Publishing Group, pp. 1225–1235. ISSN: 2157-846X. DOI: `10.1038/s41551-022-00916-z`. URL: `https://www.nature.com/articles/s41551-022-00916-z` (visited on 06/18/2024).

[11] Sam Emaminejad et al. "Autonomous sweat extraction and analysis applied to cystic fibrosis and glucose monitoring using a fully integrated wearable platform". In: *Proceedings of the National Academy of Sciences* 114.18 (May 2017). Publisher: Proceedings of the National Academy of Sciences, pp. 4625–4630. DOI: `10.1073/pnas.1701740114`. URL: `https://www.pnas.org/doi/full/10.1073/pnas.1701740114` (visited on 05/28/2024).

[12] Christopher Legner et al. "Sweat sensing in the smart wearables era: Towards integrative, multifunctional and body-compliant perspiration analysis". In: *Sensors and Actuators A: Physical* 296 (Sept. 2019), pp. 200–221. ISSN: 0924-4247. DOI: `10.1016/j.sna.2019.07.020`. URL: `https://www.sciencedirect.com/science/article/pii/S0924424719307915` (visited on 05/27/2024).

[13] Donato Vairo et al. "Towards Addressing the Body Electrolyte Environment via Sweat Analysis:Pilocarpine Iontophoresis Supports Assessment of Plasma Potassium Concentration". en. In: *Scientific Reports* 7.1 (Sept. 2017). Publisher: Nature Publishing Group, p. 11801. ISSN: 2045-2322. DOI: `10.1038/s41598-017-12211-y`. URL: `https://www.nature.com/articles/s41598-017-12211-y` (visited on 08/31/2024).

[14] Phillip Simmers et al. "Prolonged and localized sweat stimulation by iontophoretic delivery of the slowly-metabolized cholinergic agent carbachol". In: *Journal of Dermatological Science* 89.1 (Jan. 2018), pp. 40–51. ISSN: 0923-1811. DOI: `10.1016/j.jdermsci.2017.10.013`. URL: `https://www.sciencedirect.com/science/article/pii/S0923181117306783` (visited on 08/31/2024).

[15] J. Heikenfeld et al. "Wearable sensors: modalities, challenges, and prospects". en. In: *Lab on a Chip* 18.2 (2018). Publisher: Royal Society of Chemistry, pp. 217–248. DOI: `10.1039/C7LC00914C`. URL: `https://pubs.rsc.org/en/content/articlelanding/2018/lc/c7lc00914c` (visited on 10/19/2025).

[16] Z. Sonner et al. "The microfluidics of the eccrine sweat gland, including biomarker partitioning, transport, and biosensing implications". In: *Biomicrofluidics* 9.3 (May 2015), p. 031301. ISSN: 1932-1058. DOI: `10.1063/1.4921039`. URL: `https://doi.org/10.1063/1.4921039` (visited on 10/19/2025).

[17] E. Hölzle and T. Ruzicka. "Treatment of Hyperhidrosis by a Battery-Operated Iontophoretic Device". In: *Dermatologica* 172.1 (Oct. 2009), pp. 41–47. ISSN: 0011-9075. DOI: `10.1159/000249291`. URL: `https://doi.org/10.1159/000249291` (visited on 08/31/2024).

[18] *Power generation for wearable systems - Energy & Environmental Science (RSC Publishing) DOI:10.1039/D0EE03911J*. (Visited on 09/10/2024).

[19] Brince Paul et al. "Printed Iontophoretic-Integrated Wearable Microfluidic Sweat-Sensing Patch for On-Demand Point-Of-Care Sweat Analysis". en. In: *Advanced Materials Technologies* 6.4 (2021). _eprint: https://onlinelibrary.wiley.com/doi/pdf/10.1002/admt.202000910, p. 2000910. ISSN: 2365-709X. DOI: `10.1002/admt.202000910`. URL: `https://onlinelibrary.wiley.com/doi/abs/10.1002/admt.202000910` (visited on 09/10/2024).

[20] Eric Bakker and Ernö Pretsch. "Ion-Selective Electrodes Based on Two Competitive Ionophores for Determining Effective Stability Constants of IonCarrier Complexes in Solvent Polymeric Membranes". In: *Analytical Chemistry* 70.2 (Jan. 1998). Publisher: American Chemical Society, pp. 295–302. ISSN: 0003-2700. DOI: `10.1021/ac970878h`. URL: `https://doi.org/10.1021/ac970878h` (visited on 09/27/2025).

[21] Hnin Yin Yin Nyein et al. "A Wearable Microfluidic Sensing Patch for Dynamic Sweat Secretion Analysis". In: *ACS Sensors* 3.5 (May 2018). Publisher: American Chemical Society, pp. 944–952. DOI: `10.1021/acssensors.7b00961`. URL: `https://doi.org/10.1021/acssensors.7b00961` (visited on 07/19/2025).

[22] Gastón A. Crespo. "Recent Advances in Ion-selective membrane electrodes for in situ environmental water analysis". In: *Electrochimica Acta* 245 (Aug. 2017), pp. 1023–1034. ISSN: 0013-4686. DOI: `10.1016/j.electacta.2017.05.159`. URL: `https://www.sciencedirect.com/science/article/pii/S0013468617311556` (visited on 09/27/2025).

[23] R. P. Buck et al. “Measurement of pH. Definition, standards, and procedures (IUPAC Recommendations 2002)”. en. In: *Pure and Applied Chemistry* 74.11 (Jan. 2002). Publisher: De Gruyter, pp. 2169–2200. ISSN: 1365-3075. DOI: `10.1351/pac200274112169`. URL: `https://www.degruyterbrill.com/document/doi/10.1351/pac200274112169/html` (visited on 09/27/2025).

[24] Irving L. Schwartz and Jørn Hess Thaysen. “EXCRETION OF SODIUM AND POTASSIUM IN HUMAN SWEAT”. en. In: *The Journal of Clinical Investigation* 35.1 (Jan. 1956). Publisher: American Society for Clinical Investigation, pp. 114–120. ISSN: 0021-9738. DOI: `10.1172/JCI103245`. URL: `https://www.jci.org/articles/view/103245` (visited on 08/31/2024).

[25] Eric Bakker and Ernö Pretsch. “Potentiometric sensors for trace-level analysis”. In: *TrAC Trends in Analytical Chemistry*. Trace-metal analysis 24.3 (Mar. 2005), pp. 199–207. ISSN: 0165-9936. DOI: `10.1016/j.trac.2005.01.003`. URL: `https://www.sciencedirect.com/science/article/pii/S0165993605000129` (visited on 09/27/2025).

[26] Huixin Liu et al. “Printed circuit board integrated wearable ion-selective electrode with potential treatment for highly repeatable sweat monitoring”. In: *Sensors and Actuators B: Chemical* 355 (Mar. 2022), p. 131102. ISSN: 0925-4005. DOI: `10.1016/j.snb.2021.131102`. URL: `https://www.sciencedirect.com/science/article/pii/S0925400521016701` (visited on 06/13/2024).

[27] Haowei Zhang et al. “Integrated solid-state wearable sweat sensor system for sodium and potassium ion concentration detection”. In: *Sensor Review* 42.1 (Jan. 2022). Publisher: Emerald Publishing Limited, pp. 76–88. ISSN: 0260-2288. DOI: `10.1108/SR-03-2021-0081`. URL: `https://doi.org/10.1108/SR-03-2021-0081` (visited on 06/14/2024).

[28] Carlo Maccà. “Response time of ion-selective electrodes: Current usage versus IUPAC recommendations”. In: *Analytica Chimica Acta* 512.2 (June 2004), pp. 183–190. ISSN: 0003-2670. DOI: `10.1016/j.aca.2004.03.010`. URL: `https://www.sciencedirect.com/science/article/pii/S0003267004003113` (visited on 09/27/2025).

[29] M. Villiger et al. “Evaluation and review of body fluids saliva, sweat and tear compared to biochemical hydration assessment markers within blood and urine”. en. In: *European Journal of Clinical Nutrition* 72.1 (Jan. 2018). Publisher: Nature Publishing Group, pp. 69–76. ISSN: 1476-5640. DOI: `10.1038/ejcn.2017.136`. URL: `https://www.nature.com/articles/ejcn2017136` (visited on 09/27/2025).

[30] Lindsay B. Baker and Anthony S. Wolfe. “Physiological mechanisms determining eccrine sweat composition”. en. In: *European Journal of Applied Physiology* 120.4 (Apr. 2020), pp. 719–752. ISSN: 1439-6327. DOI: `10.1007/s00421-020-04323-7`. URL: `https://doi.org/10.1007/s00421-020-04323-7` (visited on 09/27/2025).

[31] Ahyeon Koh et al. “A soft, wearable microfluidic device for the capture, storage, and colorimetric sensing of sweat”. In: *Science Translational Medicine* 8.366 (Nov. 2016). Publisher: American Association for the Advancement of Science, 366ra165–366ra165. DOI: `10.1126/scitranslmed.aaf2593`. URL: `https://www.science.org/doi/abs/10.1126/scitranslmed.aaf2593` (visited on 08/31/2024).

[32] Shaghayegh Shajari et al. “MicroSweat: A Wearable Microfluidic Patch for Noninvasive and Reliable Sweat Collection Enables Human Stress Monitoring”. en. In: *Advanced Science* 10.7 (2023). _eprint: https://advanced.onlinelibrary.wiley.com/doi/pdf/10.1002/advs.202204171, p. 2204171. ISSN: 2198-3844. DOI: `10.1002/advs.202204171`. URL: `https://onlinelibrary.wiley.com/doi/abs/10.1002/advs.202204171` (visited on 09/27/2025).

[33] Bowen Zhong et al. “Wearable Sweat Loss Measuring Devices: From the Role of Sweat Loss to Advanced Mechanisms and Designs”. en. In: *Advanced Science* 9.1 (2022). _eprint: https://advanced.onlinelibrary.wiley.c
p. 2103257. ISSN: 2198-3844. DOI: `10.1002/advs.202103257`. URL: `https://onlinelibrary.wiley.com/doi/abs/10.1002/advs.202103257` (visited on 09/27/2025).

[34] Dong-Hoon Choi et al. “A Capacitive Sweat Rate Sensor for Continuous and Real-Time Monitoring of Sweat Loss”. In: *ACS Sensors* 5.12 (Dec. 2020). Publisher: American Chemical Society, pp. 3821–3826. DOI: `10.1021/acssensors.0c01219`. URL: `https://doi.org/10.1021/acssensors.0c01219` (visited on 07/19/2025).

[35] Emma J. M. Moonen et al. “Discretised microfluidics for noninvasive health monitoring using sweat sensing”. en. In: (Dec. 2024). Publisher: Royal Society of Chemistry. DOI: `10.1039/D4LC00763H`. URL: `https://pubs.rsc.org/en/content/articlehtml/2024/lc/d4lc00763h` (visited on 07/19/2025).

[36] R. F. R. Ursem et al. “Worth your sweat: wearable microfluidic flow rate sensors for meaningful sweat analytics”. en. In: (Feb. 2025). Publisher: Royal Society of Chemistry. DOI: `10.1039/D4LC00927D`. URL: `https://pubs.rsc.org/en/content/articlehtml/2025/lc/d4lc00927d` (visited on 07/19/2025).

[37] Hamed Shamkhalichenar, Collin J. Bueche, and Jin-Woo Choi. “Printed Circuit Board (PCB) Technology for Electrochemical Sensors and Sensing Platforms”. en. In: *Biosensors* 10.11 (Nov. 2020). Publisher: Multidisciplinary Digital Publishing Institute, p. 159. ISSN: 2079-6374. DOI: `10.3390/bios10110159`. URL: `https://www.mdpi.com/2079-6374/10/11/159` (visited on 08/30/2025).

[38] Sunghyun Yoon, Jai Kyoung Sim, and Young-Ho Cho. “A Flexible and Wearable Human Stress Monitoring Patch”. en. In: *Scientific Reports* 6.1 (Mar. 2016). Publisher: Nature Publishing Group, p. 23468. ISSN: 2045-2322. DOI: `10.1038/srep23468`. URL: `https://www.nature.com/articles/srep23468` (visited on 08/30/2025).

[39] Mattia Petrelli et al. “Flexible Sensor and Readout Circuitry for Continuous Ion Sensing in Sweat”. In: *IEEE Sensors Letters* 7.6 (June 2023). Conference Name: IEEE Sensors Letters, pp. 1–4. ISSN: 2475-1472. DOI: `10.1109/LSENS.2023.3274682`. URL: `https://ieeexplore.ieee.org/document/10122131` (visited on 06/17/2024).

[40] *Vialess heterogeneous skin patch for multimodal monitoring and stimulation | Nature Communications*. URL: `https://www.nature.com/articles/s41467-025-55951-6` (visited on 08/30/2025).

[41] Tianyong Zhang et al. “Recent Study Advances in Flexible Sensors Based on Polyimides”. en. In: *Sensors* 23.24 (Jan. 2023). Publisher: Multidisciplinary Digital Publishing Institute, p. 9743. ISSN: 1424-8220. DOI: `10.3390/s23249743`. URL: `https://www.mdpi.com/1424-8220/23/24/9743` (visited on 09/27/2025).

[42] Muhammad Faiz ul Hassan et al. “Electrical Characterization of Cost-Effective Screen-Printed Sensors Based on Thermoplastic Polyurethane, Polyimide, and Polyethylene Terephthalate”. en. In: *Micromachines* 16.3 (Mar. 2025). Publisher: Multidisciplinary Digital Publishing Institute, p. 319. ISSN: 2072-666X. DOI: `10.3390/mi16030319`. URL: `https://www.mdpi.com/2072-666X/16/3/319` (visited on 08/30/2025).

[43] Ding Li et al. “Designs and Applications for the Multimodal Flexible Hybrid Epidermal Electronic Systems”. In: *Research* 7 (Aug. 2024). Publisher: American Association for the Advancement of Science, p. 0424. DOI: `10.34133/research.0424`. URL: `https://spj.science.org/doi/full/10.34133/research.0424` (visited on 08/30/2025).

[44] Alexandre Larmagnac et al. “Stretchable electronics based on Ag-PDMS composites”. en. In: *Scientific Reports* 4.1 (Dec. 2014). Publisher: Nature Publishing Group, p. 7254. ISSN: 2045-2322. DOI: `10.1038/srep07254`. URL: `https://www.nature.com/articles/srep07254` (visited on 09/27/2025).

[45] Byeong Jo Kim et al. “Highly efficient and bending durable perovskite solar cells: toward a wearable power source”. en. In: *Energy & Environmental Science* 8.3 (2015). Publisher: Royal Society of Chemistry, pp. 916–921. DOI: `10.1039/C4EE02441A`. URL: `https://pubs.rsc.org/en/content/articlelanding/2015/ee/c4ee02441a` (visited on 06/12/2024).

[46] Yu Song et al. “Wireless battery-free wearable sweat sensor powered by human motion”. In: *Science Advances* 6.40 (Sept. 2020). Publisher: American Association for the Advancement of Science, eaay9842. DOI: `10.1126/sciadv.aay9842`. URL: `https://www.science.org/doi/full/10.1126/sciadv.aay9842` (visited on 06/12/2024).

[47] Di Liu et al. “A constant current triboelectric nanogenerator arising from electrostatic breakdown”. In: *Science Advances* 5.4 (Apr. 2019). Publisher: American Association for the Advancement of Science, eaav6437. DOI: `10.1126/sciadv.aav6437`. URL: `https://www.science.org/doi/full/10.1126/sciadv.aav6437` (visited on 06/12/2024).

[48] *Biofuel-powered soft electronic skin with multiplexed and wireless sensing for human-machine interfaces | Science Robotics*. URL: `https://www.science.org/doi/full/10.1126/scirobotics.aaz7946` (visited on 06/12/2024).

[49] Itthipon Jeerapan et al. "Stretchable biofuel cells as wearable textile-based self-powered sensors". en. In: *Journal of Materials Chemistry A* 4.47 (Nov. 2016). Publisher: The Royal Society of Chemistry, pp. 18342–18353. ISSN: 2050-7496. DOI: `10.1039/C6TA08358G`. URL: `https://pubs.rsc.org/en/content/articlelanding/2016/ta/c6ta08358g` (visited on 06/12/2024).

[50] Chao Li et al. "Flexible perovskite solar cell-driven photo-rechargeable lithium-ion capacitor for self-powered wearable strain sensors". In: *Nano Energy* 60 (June 2019), pp. 247–256. ISSN: 2211-2855. DOI: `10.1016/j.nanoen.2019.03.061`. URL: `https://www.sciencedirect.com/science/article/pii/S2211285519302563` (visited on 08/31/2024).

[51] Ifra Marriam et al. "Techniques enabling inorganic materials into wearable fiber/yarn and flexible lithium-ion batteries". In: *Energy Storage Materials* 43 (Dec. 2021), pp. 62–84. ISSN: 2405-8297. DOI: `10.1016/j.ensm.2021.08.039`. URL: `https://www.sciencedirect.com/science/article/pii/S2405829721004104` (visited on 08/31/2024).

[52] Mingpeng Yang et al. "Screen-Printed Wearable Sweat Sensor for Cost-Effective Assessment of Human Hydration Status through Potassium and Sodium Ion Detection". en. In: *Micromachines* 14.8 (Aug. 2023). Publisher: Multidisciplinary Digital Publishing Institute, p. 1497. ISSN: 2072-666X. DOI: `10.3390/mi14081497`. URL: `https://www.mdpi.com/2072-666X/14/8/1497` (visited on 10/22/2025).

[53] Yasemin Gokdemir and Bulent Taner Karadag. "Sweat Testing and Recent Advances". English. In: *Frontiers in Pediatrics* 9 (May 2021). Publisher: Frontiers. ISSN: 2296-2360. DOI: `10.3389/fped.2021.649904`. URL: `https://www.frontiersin.org/journals/pediatrics/articles/10.3389/fped.2021.649904/full` (visited on 10/22/2025).

[54] Audrey Reynaerts et al. "Needle-free iontophoresis-driven -adrenergic sweat rate test". In: *Journal of Cystic Fibrosis* 21.3 (May 2022), pp. 407–415. ISSN: 1569-1993. DOI: `10.1016/j.jcf.2021.08.012`. URL: `https://www.sciencedirect.com/science/article/pii/S1569199321013539` (visited on 10/22/2025).

[55] Francesca Criscuolo et al. "All-Solid-State Ion-Selective Electrodes: A Tutorial for Correct Practice". In: *IEEE Sensors Journal* 21.20 (Oct. 2021), pp. 22143–22154. ISSN: 1558-1748. DOI: `10.1109/JSEN.2021.3099209`. URL: `https://ieeexplore.ieee.org/abstract/document/9493164` (visited on 10/15/2025).

[56] Paul Horowitz and Winfield Hill. *The art of electronics*. en. Third edition, 21st printing with corrections. Cambridge, New York: Cambridge University Press, 2024. ISBN: 978-0-521-80926-9.

[57] J.R. Rodriguez et al. "PWM regenerative rectifiers: state of the art". In: *IEEE Transactions on Industrial Electronics* 52.1 (Feb. 2005), pp. 5–22. ISSN: 1557-9948. DOI: `10.1109/TIE.2004.841149`. URL: `https://ieeexplore.ieee.org/abstract/document/1391089` (visited on 10/02/2025).

[58] Konstantinos P. Pagkalos, Orfeas Panetas-Felouris, and Spyridon Vlassis. "A Time-Mode PWM 1st Order Low-Pass Filter". en. In: *Journal of Low Power Electronics and Applications* 13.2 (June 2023). Publisher: Multidisciplinary Digital Publishing Institute, p. 32. ISSN: 2079-9268. DOI: `10.3390/jlpea13020032`. URL: `https://www.mdpi.com/2079-9268/13/2/32` (visited on 10/02/2025).

[59] F. Noveletto, P. Bertemes-Filho, and D. Dutra. "Analog Front-End for the Integrated Circuit AD5933 Used in Electrical Bioimpedance Measurements". en. In: *II Latin American Conference on Bioimpedance*. Ed. by Franco Simini and Pedro Bertemes-Filho. Singapore: Springer, 2016, pp. 48–51. ISBN: 978-981-287-928-8. DOI: `10.1007/978-981-287-928-8_13`.

[60] Goodnews Imakpokpomwan et al. "Design and Implementation of an STM32f103c8 controlled DC-DC converter for mobile charging Applications". In: *2024 IEEE 5th International Conference on Electro-Computing Technologies for Humanity (NIGERCON)*. ISSN: 2377-2697. Nov. 2024, pp. 1–5. DOI: `10.1109/NIGERCON62786.2024.10927078`. URL: `https://ieeexplore.ieee.org/abstract/document/10927078` (visited on 10/02/2025).

[61] Travis Eichhorn. "Boost Converter Efficiency Through Accurate Calculations". en. In: (2008).

[62] Minh Tri Tran et al. “EMI Reduction and Output Ripple Improvement of Switching DC-DC Converters with Linear Swept Frequency Modulation”. In: *2018 14th IEEE International Conference on Solid-State and Integrated Circuit Technology (ICSICT)*. Oct. 2018, pp. 1–3. DOI: `10.1109/ICSICT.2018.8565668`. URL: `https://ieeexplore.ieee.org/abstract/document/8565668` (visited on 10/02/2025).

[63] C.K. Chava and J. Silva-Martinez. “A frequency compensation scheme for LDO voltage regulators”. In: *IEEE Transactions on Circuits and Systems I: Regular Papers* 51.6 (June 2004), pp. 1041–1050. ISSN: 1558-0806. DOI: `10.1109/TCSI.2004.829239`. URL: `https://ieeexplore.ieee.org/abstract/document/1304961` (visited on 10/02/2025).

[64] Henry W. Ott. *Electromagnetic Compatibility Engineering*. en. John Wiley & Sons, Sept. 2011. ISBN: 978-1-118-21065-9.

[65] “PCB Design Guidelines For Reduced EMI”. en. In: ().

[66] *Flexible Printed Circuit Design Best Practices*. en. Mar. 2022. URL: `https://resources.altium.com/p/flexible-printed-circuit-design-best-practices` (visited on 08/30/2025).

[67] Milan Yogendrappa. *Flex PCB Design: Optimizing for Manufacturing*. en-US. Apr. 2024. URL: `https://www.protoexpress.com/blog/flex-pcb-design-guidelines-for-manufacturing/` (visited on 08/30/2025).

A

Appendix

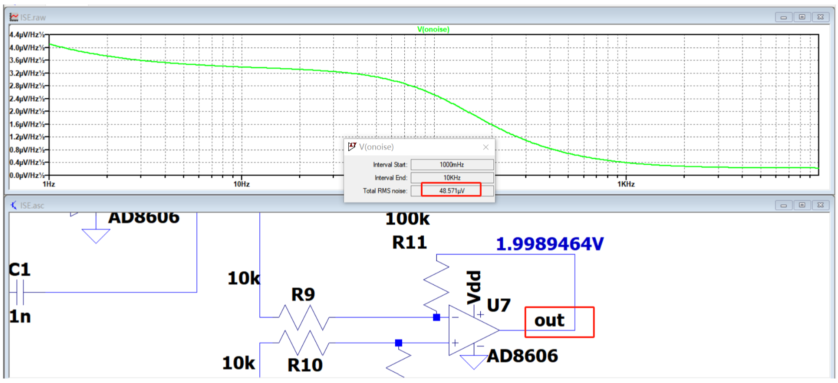

Interval Start: 1000mHz

Interval End: 10KHz

Total RMS noise: 48.571µV

Figure A.1: The noise simulation of differential amplifier output in Ltspice

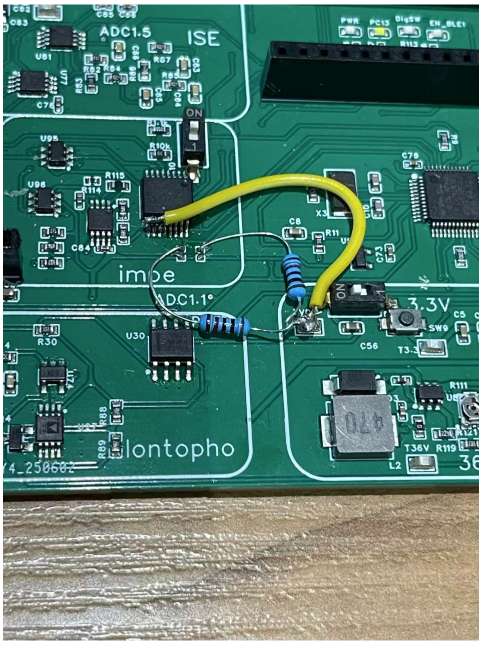

Figure A.2: Soldering the wire from 5V to 3.3V

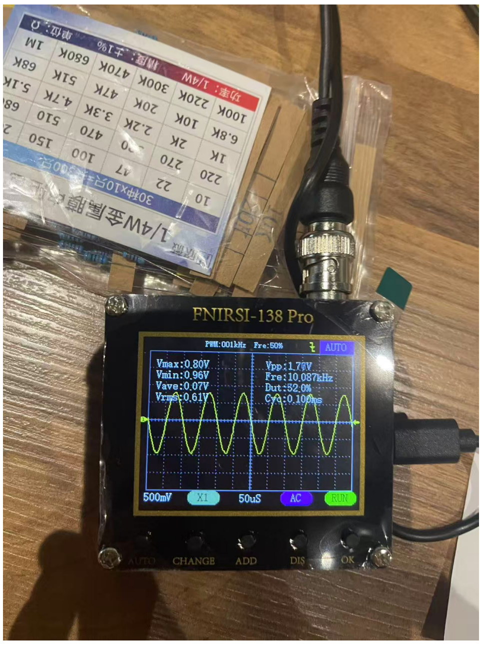

Figure A.3: sinusoidal signals were successfully observed.